Ultrafast dynamics of temporary anions probed through the prism of photodetachment

*Cate S. Anstöter, James N. Bull and Jan R. R. Verlet**

Department of Chemistry, University of Durham DH1 3LE

Contents

* e-mail: j.r.r.verlet@durham.ac.uk

Abstract

The recently developed method of frequency-, angle-, and time-resolved photoelectron imaging (FAT-PI) applied to the study of the dynamics of resonances of open-shell anions is reviewed. The basic principles of the method and its experimental realisation are outlined. The dynamics of a number of radical quinone anions is then considered. Firstly, we show for para-benzoquinone how frequency- and angle-resolved photoelectron imaging provides finger-prints of the dynamics of resonances and then how time-resolved photoelectron imaging yields deep mechanistic insight into the relaxation dynamics of the resonances. The effect of chemical substitutions of the para-quinone electrophore on the dynamics of resonances is discussed. Increasing the conjugation leads to a greatly enhanced ability for resonances to decay to the ground electronic state of the radical anion. Using time-resolved photoelectron spectroscopy, it is shown that the dynamics are facilitated by a bound valence state of the anion. The addition of electron donating methoxy groups leads to a reduced ability to access the ground state compared to para-benzoquinone. Both time-resolved dynamics and calculations provide a rationale for these observations. We consider the benefits and limitations of FAT-PI and its complementarity to 2D electron spectroscopy.

Keywords

Resonances; photoelectron imaging; electron impact; femtosecond; anion; non-adiabatic dynamics.

1. Introduction

1.1 Background and context

Electron driven processes are ubiquitous in nature and are a key tool in many technological and industrial processes.[1] Examples include: ozone chemistry initiated by chloroflouro-carbons;[2] electron transport in biology;[3,4] semiconductor etching processes;[5,6] and plasma-chemistry, -biology and -medicine.[7] In particular, low energy electron impact processes are of interest as these can initiate radical chemistry, while high energy electron impact (> 15 eV) with a neutral target leads predominantly to ionisation. Despite the broad importance of these processes, gaining a molecular level understanding of the primary events following electron capture has been challenging due to the ultrafast timescales and array of possible non-adiabatic channels. Ground state electron transfer can be described using theories such as Marcus theory,[8] but this does not account for excited states. From a fundamental perspective, the problem can be eloquently framed with the following question: How does an anion form? Consider an electron with electron kinetic energy, eKE, that impacts a neutral molecule to form an anion. In such a scenario, the total energy of the anion will be the energy of the neutral plus the eKE of the incoming electron. Even if the neutral has a positive electron affinity (i.e. can form a stable anion), the total energy of the system is always above the detachment threshold. Therefore, the anion will be metastable with respect to electron loss. These temporary negative ions (TNI) only exist for very short times because the autodetachment rate is typically less than a picosecond. Because of their fleeting lifetime, directly probing processes that occur in the detachment continuum of a TNI is a challenging task.

In the context of low eKE attachment to an isolated neutral molecule, the electron capture is facilitated by exited states of the anion that are embedded in the continuum. Such excited states are called resonances. In the absence of resonances, the scattering process is elastic.

However, when the eKE of the incoming electron coincides with that of an anion resonance (relative to the detachment threshold), then the electron can be temporarily captured, and it is the dynamics of these resonances that ultimately determine the fate of the system. Electron scattering and transmission experiments have provided a wealth of knowledge on the decay pathways of resonances across a broad range of molecules, and these experiments combined with theory have laid much of the foundation for our present understanding of electronic resonances. It is not the aim here to review this body of work, which is extensive and spans several decades; instead the reader is directed to several excellent reviews and recent works that highlight the breath and versatility of electron impact studies.[9–20] The main purpose of the present review is to outline a different approach to studying anion resonances, based on photoexcitation rather than electron impact. A key attribute of photoexcitation is that it can be extended to the time-domain, providing a new and versatile handle on probing the non-adiabatic dynamics of the primary events following electron capture.

1.2 Resonances and temporary negative anions

Resonances are electronic states embedded in a continuum and as such are always susceptible to spontaneous electron loss. Although electron loss can be very fast, a potential energy barrier prevents the electron from leaving instantly. The wavefunction of an electronic resonance in a molecular anion can be viewed as the molecular orbitals that define the excited state of the anion, as well as a part that decays through in the barrier and emerges into the continuum. Therefore, a resonance has both localised valance character as well as a free electron component. The spectral width of the resonance is determined by its lifetime which can be expressed as $\Delta E \Delta t > \hbar/2$. Typically, anion resonances have lifetimes ranging from tens of femtoseconds to a few picoseconds, dependant on both the strength of coupling of the excited state to the neutral continuum and the nature of the resonance. Electronic resonances can be classified as shape resonances and Feshbach resonances. As depicted in Figure 1,

shape resonances require a single electron transition to achieve the neutral state. In contrast, Feshbach resonances require an electronic excitation in addition to the electron loss to achieve the neutral ground state configuration. The latter imposes a larger potential energy barrier and therefore has a smaller continuum contribution. In terms of their autodetachment rates, shape resonances are typically much faster than Feshbach resonances, because the excess electron simply needs only be ejected to achieve the neutral configuration, whereas electron reconfiguration concerted with ejection is required for autodetachment of a Feshbach resonance. While autodetachment is always an open channel, other molecular processes may be in competition. For example, in dissociative electron attachment, electron impact can lead to the fragmentation to yield a neutral and anionic fragment. In this processes, nuclear dynamics must occur alongside autodetachment and therefore implies that non-adiabatic processes such as internal conversion can compete with electron loss. Although in many cases, electron emission is the ultimate fate, the nuclear geometry or the character of the resonance from which the electron is emitted will evolve over the timescale of autodetachment; any such nuclear dynamics will be reflected in the eKE of the outgoing electron. Delayed autodetachment will therefore contain signatures of the resonance dynamics. In the extreme case (which we will show to be common to conjugated molecules), internal conversion to form the ground electronic state of the anion may be possible. Complete internal vibrational energy redistribution will then lead to a statistical electron loss (or dissociation) from the hot anion ground state. This so-called thermionic emission produces electrons with a characteristic very-low eKE Boltzmann distribution.[21–24]

2. Frequency-, angle-, and time-resolved photoelectron imaging (FAT-PI)

2.1 Photoelectron spectroscopy as a route to preparing anion resonances

Electron attachment to a neutral molecule, A, is facilitated by an anion resonance, $[A^-]^*$, of the corresponding neutral-electron collision:

$$A + e^- \rightarrow [A^-]^* \rightarrow \text{products.} \quad (1)$$

It is the fate of $[A^-]^*$ that determines the products. Hence, a direct probe of $[A^-]^*$ would provide the greatest insight into its decay dynamics. Electron impact studies monitor the products that contain information about the energetics and capture efficiencies of resonances and may indirectly inform on more detailed decay dynamics of $[A^-]^*$.[9–13] An alternative route to preparing $[A^-]^*$ is through photoexcitation of the ground state anion, A^-:

$$A^- + h\nu \rightarrow [A^-]^* \rightarrow \text{products.} \quad (2)$$

In order to access the same resonance, $h\nu$ should be equal to the anion binding energy in its ground state plus the energy of the electron in equation (1). This condition implies that $h\nu$ is greater than the electron affinity of A. The process in equation (2) is photoelectron (PE) spectroscopy, where the $h\nu$ happens to be resonant with some transition of the anion. Hence, the concepts of PE spectroscopy, and specifically anion PE spectroscopy,[25,26] can be used as a basis for probing the dynamics of $[A^-]^*$.

Anion PE spectroscopy is diagrammatically illustrated in Figure 2. If a photon of energy $h\nu$ is sufficiently energetic to detach an electron from the anion, the corresponding neutral and free electron is produced. Because photodetachment is essentially instantaneous with respect to the timescale of nuclear motion, the neutral is formed with a vibrational energy

content determined by the Franck-Condon factors between the anion and neutral potential energy surfaces. By conservation of energy, the remaining energy goes to the kinetic energy of the electron, eKE. Hence, the eKE of the outgoing electron contains characteristic information about the electronic and vibrational structure of the combined anion-neutral system.[27–31] One of the key advantages of PE spectroscopy over many other optical spectroscopies is that there are no stringent selection rules for photodetachment (or ionisation). However, the detachment cross sections obey scaling laws derived from scattering theory as first described by Wigner[32] and extended by Dill.[33] For anion detachment, the detachment cross section, σ, takes the functional form:

$$\sigma = \mathrm{eKE}^{l+1/2}, \tag{3}$$

where l is the orbital angular momentum of the outgoing wave. Equation (3) is often called the Wigner threshold law and shows that as $\mathrm{eKE} \rightarrow 0$, $\sigma \rightarrow 0$. Furthermore, for low eKE, the photodetachment process is dominated by low l partial waves.

The experimental measurement of the eKE distribution can be accomplished using several techniques such as: time-of-flight spectrometers (including the magnetic bottle spectrometer), hemispherical energy analysers and imaging spectrometers. It is the latter type of spectrometers that will be discussed in more detail here because of the additional information in terms of PE angular distribution that can be measured without changing any experimental parameters.

2.2 Photoelectron imaging and angular distributions

PE imaging uses the now indispensable velocity-map-imaging (VMI) methodology developed by Eppink and Parker[34], which is based on charged-particle imaging developments

by Houston and Chandler.[35] Comprehensive accounts of these as well as a summary of diverse applications have been the subject of a number of reviews.[36,37] For the purpose of this review, it suffices to accept that following laser interaction, VMI focusses charged-particles (i.e. electrons) with a given velocity vector onto a specific point on a two-dimensional plane, regardless of where the charged-particle originated within a relatively large ionization or detachment volume. Because VMI probes a velocity vector, the measurement contains information about speed (or energy) and direction. The directional information is usually with respect to a linearly polarised light field used to detach the electron. In VMI, the Newton sphere of emitted electrons is projected (crushed) onto a 2D detector. In order to characterise any anisotropy, the measurement usually employs linearly polarised light with polarisation parallel to the face of the detector. Circularly polarised light may be used, and can lead to photoelectron circular dichroism, which is sensitive to the chirality of the molecule.[38]

The PE angular distribution (PAD) is determined by the interference of the outgoing partial waves upon photodetachment.[39] In a single photon process, the PAD is a second-order Legendre polynomial and can be expressed as[40]

$$I(\theta) = \sigma/4\pi\ (1+\beta_2\ P_2(\cos\theta)), \tag{4}$$

where θ is the angle between the polarisation vector and the PE velocity vector, and β_2 is the so-called anisotropy parameter that is used to quantify the anisotropy. β_2 can range from +2 to –1 (for a single photon process). These limiting values correspond to a PAD with a $\cos^2(\theta)$ or a $\sin^2(\theta)$ distribution relative to the polarisation vector, respectively.

Although the PAD is a simple function of θ, the quantitative prediction of β_2 is currently only tractable for simple systems. Nevertheless, their measurement can provide

qualitative insight, particularly when trends are considered across a range of *hν*. As the PAD is determined by the interference pattern of the outgoing partial waves of different angular momenta or symmetry, it is sensitive to the molecular orbital from which the electron is detached. Moreover, the PAD has a slowly varying and smooth dependence on the eKE, at least in the absence of resonances and if there is only one open electronic channel (i.e. there are no neutral excited states that can be accessed). The latter situation is often the case for the detachment from radical anions because the closed-shell neutral typically has a large gap between highest occupied and lowest unoccupied molecular orbitals. Equation (3) also shows that photodetachment is dominated by low *l* partial waves at low eKE. Using this as an assumption, Sanov and co-workers have developed a qualitative framework to predict the sign of β_2 based on symmetry arguments.[41,42] More rigorous treatments, such as the use of Dyson orbitals to predict PADs,[43] are an active and promising research area, but these methods are not yet applicable to larger molecules and have not been extended to consider how resonances influence the PADs.

2.3 Frequency-resolved photoelectron imaging

Following on from the broad introduction to PE imaging, we return to the problem at hand – that of the identification and characterisation of the dynamics of anion resonances. In PE spectroscopy, direct photodetachment produces an eKE distribution that changes by the same amount as *hν*. This is shown schematically in Figure 2. Experimentally, by measuring the PE spectra as a function of *hν*, a 2D map can be produced showing how the eKE distribution changes as a function of *hν*, indicated by the false-colour plot in Figure 2. However, if *hν* resonantly forms $[A^-]^*$, then the ensuing dynamics occurring on this excited state potential energy surface can have profound consequences on the measured PE spectra (eKE distribution) and PADs. We consider the former first. With reference to Figure 2,

following photoexcitation of $[A^-]^*$, if the autodetachment lifetime is comparable or slower than nuclear dynamics on $[A^-]^*$, then the Franck-Condon factors to the neutral ground state will differ, leading to a different final internal energy content of the neutral. By conservation of energy, such dynamics must be reflected in the PE spectrum. Thus, by scanning the *hv* across the detachment continuum and monitoring the PE spectrum at each *hv*, one may hope to observe signatures of resonances and their associated dynamics, as shown pictorially in Figure 2. Such a series of spectra, presented as a two-dimensional plot, are known as a set of frequency-resolved PE spectra.

As *hv* increases and only the direct photodetachment channel is available, the maximum eKE will increase by the same amount – i.e. the adiabatic and vertical binding energy remains constant. In Figure 2, the dashed and dotted lines of gradient 1 signifies the maximum eKE and vertical detachment energy as a function of *hv*, which can be extrapolated to yield the adiabatic and vertical binding energy of the anion, respectively. An additional vertical axis can be included to signify the energy above the adiabatic energy (detachment threshold), which allows direct comparison with electron transmission experiments. Dynamics of resonances are implied through changes in the eKE distribution of the outgoing electron. As photoexcitation energy becomes redistributed about other electronic and vibrational modes, the kinetic energy available to any subsequent autodetachment electron will be reduced and lead to a delayed autodetachment signal that is generally on the lower eKE side of the dashed line.

If the autodetachment dynamics are very fast (e.g. a short-lived shape resonance) compared to nuclear dynamics on the anionic excited state, then the PE spectrum may have the appearance of a direct photodetachment spectrum, retaining the Franck-Condon profile of the anion-to-neutral ground state detachment. In this case, one would be blind in the PE spectrum to the presence of a resonance. However, measurement of the relative

photoexcitation cross section as a function of *hv* by monitoring the total electron yield can provide evidence of resonance photoexcitation.

Frequency-resolved PE spectroscopy represents a half-reaction version of 2D electron impact spectroscopy, which has been used to study N_2, CO_2, C_3H_3N,[44–46] and a number of additional molecules over the past few months.[47] In 2D electron spectroscopy, both electron transmission and electron energy loss spectroscopy are performed, producing a 2D plot of electron yield as a function of incoming eKE and outgoing eKE. The incoming eKE is analogous to *hv* minus the adiabatic detachment energy, while the outgoing eKE is analogous to the electron binding energy in PE spectroscopy. The latter means that low electron loss values correspond to high eKE in the PE spectroscopy. The absence of electron energy loss reflects elastic collisions, which are analogous to direct photodetachment in PE spectroscopy. While the two experimental approaches possess many analogies, there are also important differences. Firstly, the geometry of the targets is different: in 2D electron spectroscopy, the electron attachment is to a neutral molecule in its equilibrium geometry, whereas frequency-resolved PE spectroscopy starts with the anion geometry. Secondly, selection rules differ between electron impact and photoexcitation. However, at sufficiently high energies above the adiabatic energy, electron impact excitation is loosely governed by conventional electric dipolar terms, resulting in behaviour similar to photoexcitation.[1] Spin selection rules differ between electron impact and photoexcitation.

Frequency-resolved PE imaging can also provide useful information through the PADs. Sudden changes in the PAD as a function of *hv* may be anticipated if resonances are excited for two reasons. Firstly, the molecular orbital from which the electron is detached has changed. Secondly, the excitation of the resonance will have an associated transition dipole moment with it such that the photoexcitation may lead to some initial alignment in the laboratory frame. These detachment properties can influence the observed PADs provided the

detachment is fast with respect to molecular rotation, which is usually the case owing to the ultrafast nature of resonance autodetachment. Such changes have been observed in a number of anion photoelectron imaging experiments.[48,49] Sudden changes in PAD as a function of eKE can also be indicative of different resonances contributing at different eKE that may result from dynamics in the continuum at a specific *hv*. Hence, the 2D nature of frequency resolved PADs can yield significant insight into the dynamics of resonances. However, the observation of no change in PAD does not mean that there were no changes in electronic state and/or excitation of a resonance. In fact, it is common for PADs to be predominantly isotropic, particularly for large and low-symmetry anions, and regardless of any dynamics occurring in the continuum.

The dimension afforded by PADs has no strict analogue in electron spectroscopy. However, velocity map imaging has been applied to electron impact studies and specifically provides insight into dissociative electron attachment processes as the anionic fragment can be velocity-mapped with respect to the incoming electron beam, providing detailed information about the dissociative electron attachment dynamics and energy distributions in the fragments.[16,18,50,17]

2.4 Time-resolved photoelectron imaging

In addition to the eKE and *hv* dimensions of frequency-resolved PE imaging, the use of lasers to photoexcite resonances allows for the straightforward extension to the time-domain using time-resolved PE imaging. There have been a number of reviews on time-resolved PE imaging and spectroscopy to which the reader is referred for a detailed discussion.[51,52] Here, a brief overview is provided with a focus on time-resolved PE imaging of anionic resonances.

The basic principles of the technique are pictorially represented in Figure 3. An ultrashort pump laser pulse is used to photoexcite the anion to a resonance. Nuclear dynamics and autodetachment ensue; a second delayed ultrashort probe pulse probes these dynamics. By

varying the time delay between the pump and probe pulses, the temporal evolution of the PE spectra can be monitored, providing a direct measure of the dynamics. Since PE spectroscopy is not restricted to specific selection rules, the dynamics of the entire reaction coordinate can be monitored.

The time-resolved dynamics are reflected through changes in the PE spectra as a function pump-probe delay. Specifically, the PE spectrum is determined by the differences in energy between the anionic resonance and the final neutral potential energy surfaces as a function of the nuclear coordinate. That is, if the final state remains the same, then dynamics are probed by the changes in Franck-Condon factors to the neutral state.[51] If more than one neutral state is energetically accessible and the dynamics involve multiple resonances (i.e. internal conversion), then the final state(s) accessed by photodetachment may differ. This idea has been used extensively used in interpreting time-resolved PE spectroscopy of bound states.[53] For resonances of radical anions, the energy gap of the closed-shell neutral is typically more than a few eV so that often, only a single final state needs to be considered for resonances a few eV above the neutral.

The dynamics of a resonance will generally involve two main decay mechanisms, autodetachment and internal conversion. Fluorescence can be ignored because of its much longer lifetime (nanoseconds). The population of a resonance may thus be probed through depletion induced by the probe, and through the new (higher energy) PE signal appearing as a result of the probe; see Figure 3. If the ultimate fate of the system is loss of an electron on a timescale shorter than that offered by the experimental arrangement, then the total PE signal will be constant as a function of time. This means that a differential measurement, such as PE imaging is crucial – an integral measurement (e.g. time-resolved electron yield) will not provide any dynamical information!

As both autodetachment and internal conversion are competing decay channels from a resonance, the observed rate of decay is equal to the sum of the individual rates: $k_{obs} = k_{AD} + k_{IC}$. Information on the individual rates may be obtained from the analysis of final state populations (see supporting information of reference 96). However, often, there is insufficient information in the spectra to determine the individual lifetimes.

Ideally, one would seek to perform time-resolved PE imaging at every *hv*. However, because time-resolved measurements typically take many hours, the total experimental time required to perform FAT-PI over a range of a few eV above-threshold with sufficiently small increments in *hv* is not practical. Therefore, time-resolved measurements are performed at specific *hv* that correspond to regions over which signatures of interesting dynamics were identified in the frequency-resolved PE spectra.

Finally, it is worth noting that, through PE imaging, the PADs are also concurrently measured as a function of time and eKE. Time-dependent PADs can be informative and may reflect changes in electronic structure[54] or population[55] as a function of time. However, very good signal levels are required to observe such changes convincingly. Nevertheless, time-dependent changes in PADs have been observed and have been exploited to provide detailed mechanistic insight into non-adiabatic dynamics.[52,56]

2.5 Experimental considerations

Several different experimental arrangements can be envisaged in applying FAT-PI to study radical anions. All arrangements have a source of anions, a mass-selection stage to isolate a specific *m*/*z*, a velocity-map imaging PE spectrometer, and light sources that can be tuned to perform frequency-resolved PE imaging and that can provide femtosecond time-resolution to perform time-resolved PE imaging. Although different arrangements will be briefly noted, we will focus on our own instrument, schematically shown in Figure 4, which couples electrospray ionisation (ESI) with FAT-PI.

Any anion source is, in principle, suitable and the choice will ultimately depend on the anion that one wishes to study. Our choice of ESI was primarily driven by our desire to study large complexes that could be probed by time-resolved PE imaging,[57–60] including dianions.[61–64] The focus here is on radical anions and actually, ESI is not the most ideal source as it tends to deprotonate molecules and form closed-shell anions. Nevertheless, the versatility of ESI is very appealing and, with care, radical anions can be readily generated in many cases. One of the major advantages of electron photodetachment of an anion compared to electron attachment to a neutral is that the former allows for prior mass-selection. That is, a single *m*/*z* can be isolated and studied even though the ions source might (and generally will) generate a range of species. The use of ESI in mass spectrometry is very common[65] and will not be reviewed here. Because laser spectroscopy and in particular time-resolved spectroscopy are used, there is an inherent need to employ pulsed light sources. Coupling a continuous ESI source to FAT-PI therefore benefits significantly from an ion storage stage, be it before, during, or after mass selection. In our experiment, we chose to use time-of-flight mass spectrometry in which the ion packet is temporally and spatially focussed in a field free region to provide high ion densities.[66] A ring-electrode trap accumulates ions and ion bunches are inject collinearly into the time-of-flight mass spectrometer at rates ranging from 10 to 1000 Hz. The collinear injection simplifies the arrangement at the expense of a modest loss of mass-resolution. In recent years, cryogenic ion traps have become popular as a means of cooling the ions (removing internal energy).[67,68]

The VMI spectrometer is situated at the field-free focus of the time-of-flight mass spectrometer. The most straight forward VMI setup is that first described by Eppink and Parker, which is made of three electrodes (extractor, repeller, ground).[34] In our VMI setup, both extractor and accelerator are held at the same potential and the acceleration field is provided by a resistive glass tube that connects to the front of the detector, which is held at

ground.[69] This VMI arrangement was implemented so that the primary ion beam is only slightly deflected as it traverses the VMI region, which means that the time-of-flight spectrum (or depletion) can continuously be measured on a shot-to-shot basis as well as allowing normalization relative to ion signal.

In the VMI assembly, a position sensitive detector is situated at the velocity-mapping focal plane. The position sensitive detector is typically comprised of a pair of microchannel plates (MCP) coupled to a phosphor screen. The interior surface of the microchannels is coated with a low work function material that converts the impact of a charged particle to an electron avalanche (typical gain of ~10^6 across two MCPs). As the electron avalanche leaves the second MCP, it is projected onto a phosphor screen, which induces phosphorescence. A thin coating of the phosphorescent material on a vacuum compatible window allows the phosphorescence to be observed from the back-side (i.e. outside the vacuum), much like an analogue oscilloscope. The phosphorescence is monitored using a charge-coupled device or similar imaging camera. Because only a few microchannels are activated by the impact of a single charged particle, the electron avalanche is localised so the velocity-mapping coordinates are transferred to the phosphor screen.

An important caveat of MCP detectors relevant to PE imaging is that care must be taken to avoid saturation of the microchannel plates. Because MCPs have large electrical resistance and long RC time constants, when too much charge is extracted from a localised region of the detector, the gain characteristics for the next amplification event may be decreased. This results in a non-linear scaling of the observed phosphorescence with PE signal, generating erroneous relative abundances of features in the PE spectra. The saturation problem is particularly acute when thermionic emission is present because this yields intense electron signal near eKE = 0 eV. As we will show in the case studies in section 3, near-zero eKE electron signal is an important indicator of non-adiabatic dynamics in anion PE spectroscopy

and, unlike conventional time-of-flight detection methods (e.g. magnetic bottle), VMI has no inherent bias to measuring such electron signal.

The raw VMI images correspond to the 3D distribution of photodetached electrons that have been crushed onto a 2D plane. If an axis of cylindrical symmetry is present, which is usually provided by linearly polarized laser light parallel to the face of the detector, then the 3D distribution can be recovered using numerical reconstruction methods post data acquisition.[70–72]

FAT-PI requires the combination of broadly tuneable laser light for single-photon frequency-resolved measurements and femtosecond laser pulses for time-resolved measurements. In our set-up, the tuneable (200 – 2800 nm) laser light is provided by a Nd:YAG pumped optical parametric oscillator. For the time-resolved dimension, a commercial Ti:Sapphire amplified femtosecond laser is used. The femtosecond pulses are divided into pump and probe paths using beam splitters and delayed relative to each other with a motorised delay stage. For pump pulses, the fundamental ($h\nu$ = 1.55 eV) or harmonics thereof can be used, or some degree of tuneability can be achieved by use of an optical parametric amplifier. The probe is usually the fundamental, $h\nu$ = 1.55 eV (800 nm). Pump and probe pulses are combined and loosely focussed into the interaction region. Tight focussing can increase PE signal, but at the expense of undesirable non-linear effects. The temporal resolution of the experiments is determined by the cross-correlation of the pump and probe pulses, which is ~60 fs for a 3.10 + 1.55 eV pump-probe experiment in our set-up. One of the appealing aspects of probing dynamics in the continuum is that the fundamental is always sufficient probe resonances. Further, because electron emission is usually the ultimate fate following photoexcitation, the depletion of PE features arising from delayed emission provides a measure of the ground state recovery dynamics. Thus, there is no requirement to

use *hv* that are in excess of the electron affinity to probe recovery of the ground electronic state of the anion.

3 Para-benzoquinone as an electrophore

3.1 Background

Over the past few years, we have developed and employed the technique of FAT-PI to study the dynamics of a range of anion resonances in quinones. Para-benzoquinone (pBQ) is a central moiety found in many quinone derivatives ubiquitous in nature. The structure of pBQ is shown in Figure 5(a). Quinones are found in biological electron-transfer chains,[73–75] the most prominent examples being plastoquinone and ubiquinone. Plastoquinone is the terminal electron acceptor in type II photosynthetic reaction centres,[3,76] while ubiquinones act as dynamic electron shuttles between protein chains of the mitochondria respiratory chain.[77] Quinones are integral components of these biological systems due to their unique electron accepting properties that can be attributable to thermodynamically favourable electron attachment processes leading to stable charge separated states in photochemical reactions. The widespread use of quinones in nature has seen their incorporation in bioinspired electron-transfer systems, mimicking photosynthetic reaction centre functions.[78,79]

The electron-transfer reactions of pBQ can be highly exergonic. As such, these reactions often fall into the Marcus inverted region[80] where electron transfer is inhibited by a free energy barrier. However, experimental electron transfer rates to several quinones show strong deviations from Marcus theory behaviour[8,81] with time-scales several orders of magnitude faster, suggestive of a barrierless pathway. Such fast electron transfer rates can potentially be rationalised by the presence of low-lying anionic resonances that act as a door-way electron acceptor state, which subsequently decays to the ground state.

Due to the ubiquity of pBQ in electron transport chains and the possible role of excited states of its radical anion, there have been a range of studies[82–108] focusing on the electronic states of the neutral and radical anion. Most of the initial identification of pBQ^- resonances was attained through electron attachment and transmission studies. [82,83,92–94] These studies have established that the equilibrium geometry of pBQ^- is planar and of D_{2h} symmetry with a $^2B_{2g}$ ground state produced by the addition of an electron to the lowest unoccupied π^* molecular orbital. Closed-shell neutral pBQ also has a planar D_{2h} equilibrium geometry with a ^1A_g electronic ground state. pBQ^- does not support any valence-bound excited states. There are, however, a number of low-lying π^*-resonances. Three bright resonances have been assigned as ^2A_u, 2^2B_{3u}, and 3^2B_{3u}. The first two involve one-electron excitations, corresponding to the promotion of an electron from the $b_{2g} \rightarrow a_u$ and $b_{3u} \rightarrow b_{2g}$ molecular orbitals, respectively. Therefore, the ^2A_u state is a shape resonance, while 2^2B_{3u} is predominantly of Feshbach character (see Figure 1). The 3^2B_{3u} resonance is of shape character, and is situated around 2.1 eV above the anion ground state.

The most accurate determination of the adiabatic electron affinity of jet-cooled pBQ^- is 1.860 eV ± 5 meV by Schiedt and Weinkauf using photodetachment spectroscopy.[87] Their photodetachment yield spectra recorded over the $2.07 < h\nu < 2.56$ eV range are shown in Figure 6(a). The series of weak but sharp peaks that were assigned to vibrational states of the optically dark $^2B_{2u}$ and $^2B_{3g}$ Feshbach resonances at 2.27 and 2.41 eV above the anion ground state, respectively. A lifetime of ~1 ps was inferred from the peak widths, which is consistent with their Feshbach character. A much broader peak in the photodetachment yield spectrum at ~2.5 eV above the anionic ground state was identified as the 0-0 transition of the ^2A_u resonance. Again, the width inferred a lifetime of 25 fs, which is consistent with the shape character of the ^2A_u resonance. A low-resolution photodetachment spectrum spanning a broader range is shown in Figure 6(b), which allows identification of the overlapping ^2A_u and

2^2B_{3u} resonance features as well as an intense feature corresponding to the bright 3^2B_{3u} resonance.[88,89,95]

Schiedt and Weinkauf also characterised a series of changes in vibrational structure upon exciting specific resonances. Examples are shown in Figure 6(c). The changes in vibrational structure reflect differing autodetachment processes associated with the specific resonance by virtue of the changing Franck-Condon factors. This elegant experiment clearly demonstrated the subtle effects observable in the PE spectra following the excitation of anion resonances, which was enabled by the high resolution of their measurements. However, their study considered only a very narrow spectral range; there is generally a trade-off between resolution and dynamic-range. Our interest was in characterising the dynamics deeper into the continuum – spanning a range similar to that shown in Figure 6(b) – albeit with reduced resolution.

3.2 Above-threshold dynamics probed by FAT-PI

Figure 7(a) and (b) shows the results from frequency and angle-resolved PE spectroscopy, respectively, over the $2.48 < h\nu < 4.59$ eV range.[90] This range probes the continuum between 0.62 eV to 2.73 eV above the ^1A_g neutral ground state. Each PE spectrum has been normalised to accentuate changes in the PE spectra, but could equally be normalised using the relative excitation cross section data from Figure 6(b). For $h\nu > 3.5$ eV the PE spectra take the appearance of a conventional direct PE spectrum and the $h\nu = 4.59$ eV closely resembles the high resolution PE spectrum taken by Wang and co-workers at $h\nu = 4.66$ eV.[91] The signal at low eKE for $h\nu > 4.2$ eV arises from formation of neutral excited states.[91] The 3^2B_{3u} resonance has little influence on the eKE distributions. Close inspection, however, reveals a very small deviation from the direct photodetachment peak towards lower eKE. This points to a very rapid autodetachment process that mostly preserves the Franck-Condon factors to ^1A_g, which is consistent with the shape character of 3^2B_{3u}.

The frequency-resolved PE spectra clearly show that at $h\nu$ ~ 2.9 eV, there is a dramatic increase in signal around eKE ~0.2 eV, implying a strong deviation from direct photodetachment. The PE spectrum at $h\nu$ = 3.10 eV, shown in Figure 8, highlights this feature as well as identifying a small PE peak situated at eKE ~ 0 eV. The feature at zero eKE is unexpected in anion PE spectroscopy for direct photodetachment because of Equation (3), thus suggesting an indirect detachment process such as thermionic emission. Indeed, electron attachment experiments have observed pBQ^- formation with an electron detachment lifetime of many μs,[92–94] supporting existence of a thermionic emission channel. The thermionic emission peak is visible in Figure 7(a) for 2.5 < $h\nu$ < 3.2 eV and implies that excitation of resonances in this $h\nu$ range leads to the reformation of ground electronic state pBQ^-.

The angle-resolved PE spectra in Figure 7(b) provide further support for the presence and dynamics of resonances. Note that the β_2 parameters are only shown where there is sufficient PE signal. With increasing $h\nu$, at $h\nu$ ~ 2.75 eV there is a sudden change in β_2 from +0.2 to 0.0 in the 0.2 < eKE < 0.5 eV range. These changes in the PAD are interpreted to reflect a sudden change in photoexcitation character and detachment dynamics. Additionally, between 2.75 < $h\nu$ < 3.2 eV, there is a change in β_2 as a function of eKE. For eKE < 0.5 eV, β_2 is essentially zero, while for eKE > 0.5 eV β_2 is slightly negative. Electronic structure calculations support that the ^2A_u and 2^2B_{3u} resonances are vertically situated in this range[85,86,90,109] in accord with photodetachment yield spectra[88,89,95] that showed that both have broad and overlapping absorption profiles with oscillator strengths much greater than direct photodetachment into the continuum.

The PE spectrum at $h\nu$ = 3.10 eV (Figure 8) is representative of the dynamics occurring in the 2.7 < $h\nu$ < 3.2 eV range. We suggested that at $h\nu$ = 3.10 eV, the 2^2B_{3u} resonance was predominantly excited, but that the close lying ^2A_u state was involved in the relaxation dynamics. Specifically, we proposed that the 2^2B_{3u} resonance could undergo internal

conversion to populate the ^2A_u resonance. This mechanism was plausible because 2^2B_{3u} is a Feshbach resonance and may be expected to survive sufficiently long to allow internal conversion. From Figure 8, the peak at eKE ~ 0.2 eV (^2A_u) is more intense than the high-eKE peak (2^2B_{3u}) because the internal conversion dynamics are faster than 2^2B_{3u} autodetachment. The ^2A_u state is a shape resonance with an inferred autodetachment lifetime of 25 fs, so it is expected that most ^2A_u population undergoes autodetachment leading to a PE feature peaking around eKE ~ 0.2 eV. However, the minor thermionic emission peak centred at eKE = 0 eV shows that some population can recover the ground electronic state.

The above hypothesis was tested using time-resolved measurements in which a 3.10 eV pump pulse excites the 2^2B_{3u} resonance and a delayed 1.55 eV probe was used to track the population dynamics by time-resolved PE imaging. Figure 9(a) shows two pump-probe PE spectra.[109] In the $t < t_0$ spectrum, the probe arrives before the pump, while both femtosecond pulses are overlapped in time in the $t = t_0$ spectrum. The $t < t_0$ spectrum is identical to the $h\nu$ = 3.10 eV PE spectrum because the probe is not resonant with any transition and has insufficient energy to detach an electron from ground electronic state pBQ^-. When pump and probe pulses are overlapped, the PE spectrum shows a new feature at higher eKE as well as some depletion of the single-photon peak around eKE ~ 0.2 eV. The kinetics of these two features was tracked by integration of the PE signal over their respective spectral windows. The kinetics of the high eKE pump-probe appearance feature mirrors that of the depletion feature, as shown in Figure 9(b). The extracted lifetimes are < 40 fs and limited by the time-resolution of the experiment. Closer inspection of the high eKE pump-probe feature reveals a spectral shape similar to the $h\nu$ = 3.10 eV spectrum, but blue-shifted by the probe photon energy (1.55 eV). Hence, by integrating over the features assigned to result from 2^2B_{3u} and ^2A_u autodetachment, the kinetics of individual resonances can be extracted (see Figure 9(b)). The results of this integration is shown in Figure 9(c), showing that the lower eKE feature

(^2A_u autodetachment) has a delayed appearance time of ~ 20 fs, corresponding to the $^2B_{3u} \rightarrow {}^2A_u$ internal conversion dynamics. The depletion of the PE signal around eKE ~ 0.2 eV arises because the probe pulse removes population that would otherwise either undergo internal conversion or autodetachment – see Figure 3.

The kinetics observed in Figure 9 represent a competition between autodetachment and internal conversion dynamics. The ~20 fs delay in ^2A_u appearance observed in Figure 9(c) can be associated with the $2^2B_{3u} \rightarrow {}^2A_u$ internal conversion and can be modelled using a simple sequential model in which the 2^2B_{3u} state internally converts with lifetime, τ_B, and subsequently the ^2A_u state decays (primarily by autodetachment) with lifetime τ_A. The populations of the 2^2B_{3u} and ^2A_u states, which are probed in the time-resolved PE spectra, can be written as:

$$N_B(t) = \exp(-t/\tau_B),$$

$$N_A(t) = \{\tau_B^{-1}/(\tau_A^{-1} - \tau_B^{-1})\}\ \{\exp(-t/\tau_B) - \exp(-t/\tau_A)\}. \qquad (5)$$

By convoluting Eq. (5) with a Gaussian to represent the time-resolution of the experiment, the experimentally observed shift ~20 fs can be modelled. This procedure revealed that τ_A = 27 fs as $\tau_B \rightarrow 0$ and, therefore, the ^2A_u lifetime must be less than 27 fs. This result is consistent with the ~25 fs lifetime inferred from Figure 6(a) for the ^2A_u resonance.[87] As 25 fs this is a minimum lifetime (because of the Uncertainty Principle), a similar analysis based on Eq. (5) suggests that the $\tau_B < 30$ fs. Of course, these lifetimes are all approximate because of the approximate nature of the measured 20 fs shift. Nevertheless, the modelling demonstrates the level of insight that can be attained from the time-resolved measurements.

Electronic structure calculations, summarised in Figure 10, were performed to explore the feasibility of the proposed internal conversion.[109] A conical intersection (CI) between the 2^2B_{3u} and ^2A_u states was identified as well as a number of additional CIs between other states. Importantly, two CIs leading to internal conversion to the lower-lying Feshbach resonances were also identified, providing a potential route to the ground electronic state and the observed thermionic emission channel. Because the principal Franck-Condon modes are also the modes required to reach the $2^2B_{3u}/^2A_u$ CI geometry, an efficient internal conversion might be expected. More recent calculations at higher level of theory broadly agree with the above interpretations and highlight that several decay routes may coexist.[86] These calculations also semi-quantitatively account for the observations in the frequency and angle-resolved PE spectra over the $2.5 < h\nu < 3.2$ eV range and similarly assign the feature at eKE ~ 0.2 eV to the autodetachment from the ^2A_u resonances.

4. Effect of substituents on non-adiabatic dynamics

One of the primary goals of spectroscopy is of gas-phase to develop a bottom-up approach to studying structure-function relationships. There are many cases in the literature that demonstrate a bottom-up approach. Examples include the dynamics of nucleobases to nucleotides[110] and oligonucleotides and the dynamics of excess electrons in solvent clusters,[111,112] for which the extrapolation to the bulk has recently been demonstrated.[113]

As described above, pBQ is a common structural motif in natural and artificial electron acceptors. Therefore, in the same vein as a chromophore is the molecular unit that absorbs light, pBQ can be thought of as the electrophore in more complex electron acceptors. A natural question that arises is: how does pBQ's electron accepting ability change as it becomes substituted? From an isolated molecule perspective, we can consider how the dynamics of resonances are modified by structural changes. In nature, two of the main families of electron acceptors incorporating pBQ are the vitamin Ks and the coenzyme Q

series. Using FAT-PI, we have studied how these structural changes modify the dynamics of anionic resonances, providing a bottom-up understanding of these families.

4.1 Extended conjugation: Menadione

The effect of increased conjugation with the para-quinone ring is considered first. The addition of an aromatic ring leads to an enhanced delocalisation of the π-system, which is expected to have a profound impact on the resonance dynamics. The molecule shown in Figure 5(b) is menadione (2-methyl-1,4-naphthoquinone) or commonly known as vitamin K_3 and abbreviated as MD. MD is the key structural sub-unit in the naturally-occurring vitamins K_1 and K_2 where an aliphatic chain attached to the pBQ unit increases solubility in lipid membranes. Like other quinones, vitamin Ks play integral roles as electron acceptors in electron transport chains of both photosystems and mammalian cells.

The radical anion of menadione, MD^-, may be expected to exhibit resonances and dynamics analogous to those of pBQ. However, the extended conjugation results in an increased density of π states and thus π* resonances. Experimentally, MD was generated as a radical anion using ESI conditions similar to those for pBQ^-. The frequency-resolved PE spectra of MD^- are shown in Figure 11[114] and can be compared to those for pBQ^- shown in Figure 7(a). Again, each PE spectrum has been normalised to its integrated signal in order to accentuate trends across spectra.

The frequency-resolved PE spectra of MD^- show four main trends across the photoexcitation range. Firstly, at all *hν*, there is a strong thermionic emission signal, with maxima around *hν* ~ 2.0 and ~ 3.0 eV. Secondly, a prompt detachment feature that has an eKE increasing commensurate with *hν* is present for 2.0 > *hν* > 2.7 eV and 3.5 > *hν* > 4.5 eV. This feature contains contributions from both direct photodetachment and prompt autodetachment. Thirdly, a broad feature consistent with delayed autodetachment appears at a fixed eKE centred at ~ 0.25 eV, which is most evident between 3.0 > *hν* > 3.75 eV. Finally,

at the highest excitation energies ($h\nu$ > 4.0 eV), a new low-eKE feature emerges that was assigned to direct photodetachment to excited states of the neutral.

The key observation is that, over the first 3 eV of the continuum, thermionic emission dominates. In fact, the true relative thermionic emission yield is much higher than determined by these PE spectra because the thermionic emission yield was only measured for ~100 ns after photoexcitation; thermionic emission typically operates over a microsecond timescale. Based on a thermionic emission lifetime of 10 μs, which was estimated from a series of electron attachment experiments considering similar conjugated quinones,[115,116] our experiments measured only few percent of the total thermionic emission yield. Therefore, the dominating thermionic emission signal indicates that there exists very efficient internal conversion pathways linking resonances embedded in the continuum to the ground electronic state.

The frequency-resolved PE spectra suggest that the efficiency in reforming the ground electronic state is highest around $h\nu$ ~ 3.0 eV, as evidenced by the fact that there is almost no direct photodetachment into the continuum. Time-resolved PE imaging with a 0.95 eV (1300 nm) probe was used to gain mechanistic insight into the ground state recovery dynamics following photoexcitation of the resonance at $h\nu$ = 3.10 eV. Figure 12(a) shows two time-resolved PE spectra for $t < t_0$ (i.e. probe before pump) and at t = 50 fs. The former is essentially identical to the single colour PE spectrum at 3.10 eV because the pump is not resonance with any transitions in the system. At t = 50 fs, three spectral changes are observed: depletion of the thermionic emission feature at low eKE; the appearance of a PE feature around eKE ~ 0.6 eV; and the appearance of a high-eKE PE feature centred at ~ 1.8 eV. The feature at eKE ~ 1.8 eV is only present for the first 100 fs. The contributions of each of the three pump-probe features were extracted by fitting all the time-resolved PE spectra to a three-channel model and the amplitudes of these fits are shown in Figure 12(b). The

kinetics show that the feature at eKE ~ 1.8 eV (A3) rapidly decays with a concurrent rise in the feature at eKE ~ 0.6 eV (A2). In turn, the feature at eKE ~ 0.6 eV decays on a ~800 fs timescale with a concomitant recovery of the thermionic emission depletion (A1). The recovery of the thermionic emission depletion signifies a recovery in the ground electronic state population.

The transient population of the resonance that is initially photoexcited at 3.10 eV can be correlated with the time-resolved PE feature at eKE ~ 1.8 eV (A3) that decays on a <100 fs timescale. From the time-resolved PE spectra, the resonance population decays into an intermediate (A2), which has a lifetime of 800 fs. The appearance of an intermediate is not surprising, but a lifetime of ~800 fs would be very long for a resonance that appears to decay almost exclusively to the ground electronic state. However, the intermediate feature (A2) peaks at eKE ~ 0.6 eV (from a 0.95 eV probe pulse energy), suggesting that the intermediate might be vertically bound.

To further investigate the intermediate (A2), a second set of time-resolved experiments employing a 3.10 + 1.55 eV pump-probe scheme were performed. In the forward direction (3.10 eV pump), the same sequence of time-resolved dynamics were observed as with a 0.95 eV probe, as shown in Figure 12(c). However, time-resolved dynamics were also observed in the reverse direction, where the 1.55 eV serves as the pump pulse while the 3.10 eV as the probe pulse. A 1.55 eV pump pulse is insufficient to access resonances and therefore, the excited state probed in 'negative' time must be due to a bound electronic state. This second set of time-resolved measurements determined the lifetime of the bound state to be 800 fs, supporting assignment as the intermediate state (A2) in the forward direction. This bound state then undergoes internal conversion to the ground electronic state, although the rate is now less important because autodetachment is no longer an open channel.

Electronic structure calculations supported the above observations and identified a number of relevant resonances as well as the bound state. In a simple correlation diagram shown in Figure 13(a), MD can be viewed as being compromised of pBQ (or methyl-8pBQ) and Z-butadiene subunits. Such a breakdown is useful in terms of building a bottom-up picture.

Based on the calculated energetics and oscillator strengths, the $3^2A''$ resonance is likely to be excited at $h\nu$ = 3.10 eV. Photoexcitation of $3^2A''$ involves migration of electron density from the Z-butadiene to the pBQ subunit, while photoexcitation of $2^2A''$ involves electron migration from a molecular orbital localised on the pBQ subunit to delocalised orbitals over the entire molecule. We note that due to the ultrafast timescales and broad eKE distributions, the time-resolved measurements do not inform if the $2^2A''$ resonance is involved in the dynamics as an intermediate. Regardless, internal conversion from the $3^2A''$ (and/or $2^2A''$) resonance leads to the $1^2A''$ bound electronic state, which also has strongly delocalised character across the entire π-system.

The key influence of the increased conjugation in MD^- compared with pBQ^- is that there is an increased density of states as well as bonding interactions leading to a bound electronic state, $1^2A''$. The bound-state is central to the ability to reach the ground electronic state because it serves as an energetically close-lying intermediate to which resonances can couple. One can hypothesise that a further increase in conjugation may lead to even more efficient ground state recovery. It is also likely the case that, due to the increase in rigidity with increased conjugation, the analogy between FAT-PI to electron capture studies will strengthen because differences in anion and neutral geometries will become less pronounced.

4.2 Electron donating groups: Coenzyme Q_0

The second structural alteration that was considered was the addition of electron donating methoxy groups and a methyl group to pBQ (although the latter has little effect). Coenzyme

Q_0 (2,3-dimethoxy-5-methyl-*para*-benzoquinone), abbreviated as CQ_0, represents the smallest member of the coenzyme Q-family. The subscript refers to the number of isoprenyl subunits in an aliphatic chain attached to the unsubstituted position shown in Figure 5(c). Similar to the vitamin K class of molecules, the isoprenyl chain enhances lipid miscibility. The most common coenzyme in nature is, CQ_{10}, also known as ubiquinone, which is commonly taken as a dietary supplement.

The frequency-resolved PE spectra are shown in Figure 14(a).[117] To assist the discussion, calculated energetics of CQ_0^- resonances are presented in Figure 15(a) alongside those for pBQ^-. The calculations show the ^2A_u and 2^2B_{3u} resonances in pBQ^- correlate with the 3^2[S] and 5^2[F] resonances in CQ_0^-, respectively, and have similar oscillator strengths. However, comparing the frequency resolved PE spectroscopy of CQ_0^- with that for pBQ^- (Figure 7(a)), the branching ratios of autodetachment and internal conversion are different. Around $h\nu \sim 3$ eV, the delayed autodetachment yield is reduced for CQ_0^- relative to that from ^2A_u autodetachment in pBQ^- (Figures 7(a) and 8). Additionally, there is very little evidence for thermionic emission in CQ_0^-. Hence, CQ_0^- appears to be less effective at retaining an above-threshold excess electron. At first glance, this result is surprising because the electronic structures of both species are very similar.

Time-resolved PE imaging using a 3.10 + 1.55 eV pump-probe scheme suggests a 5^2[F] $\rightarrow 3^2$[S] internal conversion mechanism similar to the $2^2B_{3u} \rightarrow {}^2A_u$ internal conversion in pBQ^-. However, the time-resolution was limited by the experimental cross-correlation and pump-probe features were broader and more difficult to disentangle. Therefore, additional electronic structure calculations were used in order to rationalise the experimental branching ratio differences.

One obvious difference between CQ_0^- and its pBQ^- electrophore is the reduced symmetry in CQ_0^-. The influence of reduced symmetry is reflected in the frequency-resolved PADs,

which showed similar trends in β_2 for pBQ^- and CQ_0^-, but reduced magnitude for CQ_0^-. In terms of electronic structure, the reduced symmetry and changes in bonding from the methoxy-groups alters the character of the π^* orbitals defining the resonance. These changes can be quantified through analysis of (MP2 corrected) CASSCF wavefunctions. For pBQ^-, the 2^2B_{3u} resonance is predominantly of Feshbach character with a small amount (~19%) shape character. In contrast, the analogous 5^2[F] resonance in CQ_0^- has ~41% shape character. Because shape resonances typically have shorter autodetachment lifetimes than Feshbach resonances, the reduction in $5^2[F] \rightarrow 3^2[S]$ internal conversion yield may be a consequence of a faster autodetachment rate of the initially excited 5^2[F] resonance in CQ_0^-.

The above consideration relied on electronic structure calculations at the Franck-Condon region. However, as the decay mechanism of the 5^2[F] or 2^2B_{3u} resonances involves non-adiabatic dynamics through conical intersections, the energetics and structural dynamics required to achieve these crossing points should also be considered. The relative energetics of the $2^2B_{3u}/^2A_u$ and the $5^2[F]/3^2[S]$ conical intersections in pBQ^- and CQ_0^-, respectively, are shown in Figure 15(b). While the $2^2B_{3u}/^2A_u$ conical intersection is lower in energy than the vertically excited 2^2B_{3u} resonance, the $5^2[F]/3^2[S]$ conical intersection is essentially at the same energy as the vertically excited 5^2[F] resonance. As the main Franck-Condon active modes are also those required to reach the conical intersection geometry, the potential energy gradient in pBQ^- drives population in the 2^2B_{3u} state towards the conical intersection. For CQ_0^-, the driving force to reach the conical intersection is substantially reduced, which implies that there is a higher relative probability for autodetachment. This, combined with the enhanced shape character of the 5^2[F] resonance, provides a rationale for the poorer electron accepting ability of CQ_0^- compared to pBQ^-.

5. Outlook

FAT-PI has the potential to provide a wealth of information concerning the dynamics of electron attachment. The dispersion of information in terms of photon (electron impact) energy, PE kinetic energy (electron energy loss), PE angular distributions, and time, makes FAT-PI an exceedingly information-rich methodology to probe anion resonances despite their very short lifetimes. However, as a half-reaction, PE spectroscopy does not probe the true electron impact process because the initial geometry is that of the anion and because of the differences in selection rules between photon- and electron-excitation. For these reasons, frequency-resolved PE spectroscopy is complementary to 2D electron spectroscopy. It would be interesting to compare the two methods through a combined study on a model system. At present, frequency-resolved PE spectroscopy is performed as a lower-resolution experiment in comparison to 2D electron spectroscopy. However, higher resolution can be achieved if desired, such as for pBQ^- in Figure 6.[87] The cost of higher resolution is that such experiments become extremely time-consuming as the number of PE images that need to be collected increases dramatically. Further insight about resonance energetics can be attained by recording the total PE yield as a function of *hv*, which can also provide a normalization factor for each frequency-resolved image. However, care must be taken in performing such experiments as some channels are difficult to measure such as the total thermionic emission yield and fragmentation leading to charged products, which will not appear in the PE yield spectrum. Complementary ion storage experiments can provide a means of determining the true electron yield in systems that exhibit thermionic emission over an extended timescale.

In summary, FAT-PI is a new and powerful technique to probe anion resonances and temporary anions. FAT-PI has two principal advantages. Firstly, it provides a wealth of information due to its multidimensional nature, some of which is immediately useful and some of which is potentially useful when combined with a theoretical framework. The temporal dimension allows short-lived anion resonances to be probed in real-time and, as

shown in the examples above, can be crucial in attaining a detailed mechanistic insight. PE angular distributions may yield further information; however, detailed interpretation is difficult due to the lack of easy-to-use theoretical frameworks. Because the PADs are directly linked to the molecular orbitals from which the electron is detached, the information content in the frequency-resolved PADs may provide insight into changes in electronic character with laser photoexcitation energy, while time-resolved PADs could potentially reflect changes in electronic character (e.g. resonance population) in real-time. The second major advantage of FAT-PI relates to the fact that one starts with an anion. Although starting with an anion complicates the comparison with a full electron attachment collision, because the anion is charged, mass-spectrometric techniques can be used to isolate the ion packet prior to investigation. Furthermore, a wide range of ion sources can be used to generate non-volatile anions. Together, these features mean that FAT-PI can be used to study a very wide range of species, including large molecules. For example, in addition to studying MD^-, we also performed experiments on the biologically relevant vitamin K_1 to show that the aliphatic chain has little effect on the dynamics of the resonance around $h\nu$ = 3.1 eV.[114] Very recently, we studied the dynamics in the open-shell π-stacked dimer anion of CQ_0, enabled by the fact that $(CQ_0)_2^-$ could be isolated, where we showed a new mechanism in which a valance-localised resonance internally-converts into a dipole-bound state.[118] Finally, FAT-PI is not limited to radical anions. The dynamics of resonances of closed-shell anions can be studied in the same way. As examples, we have investigated resonances of the chromophore of the green fluorescent protein,[119,120] multiply-charged anions,[64,121] and deprotonated tetracene.[122]

As a final point, it is worth commenting on the role and limitations of theory. Calculations are vital in order to gain an understanding of the electronic structure of the resonances that are excited and to explore how resonances might internally convert between one another and any bound states. Electronic structure calculations provide a standard means

of predicting bound excited states and possible dynamical pathways, however, the calculation of resonances is much more complex due to the influence of the continuum.[123] One promising theoretical approach to remedy the divergent wavefunction character of resonances in electronic structure calculations is through the addition of a complex absorbing potential (CAP) to the Hamiltonian.[124–127] CAP methods have generally been shown to provide reasonable resonance energetics and widths,[85] but are only starting to be implemented in common quantum chemistry packages. However, CAP methods still do not account for motion on the potential energy surface. A comprehensive theoretical account would require more complex dynamical simulations that include coupling to other potential energy surfaces as well as the continuum (i.e. autodetachment). It is therefore clear that there is still some way to go before theoretical methods become predictive of resonance dynamics for anything beyond very small systems.

Acknowledgment

This review represents the work of a number of students. In particular, we are grateful to Daniel Horke, Christopher West, Erkki Antonkov and Laurence Stanley. We are also grateful to Lluís Blancafort and Quansong Li for fruitful collaborations and discussions. This work has been funded by the EPSRC and the ERC (Starting Grant 306536).

References

[1] I. Shimamura and K. Takayanagi, *Electron-Molecule Collisions* (Springer US, Boston, MA, 1985).

[2] M.H. Rees, *Physics and Chemistry of the Upper Atmosphere* (Cambridge University Press, 1989).

[3] M.F. Hohmann-Marriott and R.E. Blankenship, Annu. Rev. Plant Biol. **62**, 515 (2011).

[4] J. Jortner and M. Bixon, *Advances in Chemical Physics; Electron Transfer - From Isolated Molecules to Biomolecules* (John Wiley & Sons, 1999).

[5] T.M. Figueira-Duarte and K. Müllen, Chem. Rev. **111**, 7260 (2011).

[6] X. Guo, M. Baumgarten, and K. Müllen, Prog. Polym. Sci. **38**, 1832 (2013).

[7] L.G. Christophorou and J.K. Olthoff, *Fundamental Electron Interactions with Plasma Processing Gases* (Springer US, Boston, MA, 2004).

[8] R.A. Marcus, Annu. Rev. Phys. Chem. **15**, 155 (1964).

[9] G.J. Schulz, Rev. Mod. Phys. **45**, 378 (1973).

[10] K.D. Jordan and P.D. Burrow, Chem. Rev. **87**, 557 (1987).

[11] K.D. Jordan and P.D. Burrow, Acc. Chem. Res. **11**, 341 (1978).

[12] H. Hotop, M.-W. Ruf, M. Allan, and I.I. Fabrikant, in *Adv. At. Mol. Opt. Phys.* (2003), pp. 85–216.

[13] E. Illenberger, in *Photoionization and Photodetachment*, edited by C.Y. Ng (World Scientific, Singapore, 2000), pp. 1063–1160.

[14] G.E. Caledonia, Chem. Rev. **75**, 333 (1975).

[15] E. Illenberger and B.M. Smirnov, Physics-Uspekhi **41**, 651 (1998).

[16] K. Regeta, C. Bannwarth, S. Grimme, and M. Allan, Phys. Chem. Chem. Phys. **17**, 15771 (2015).

[17] X. Wang, X. Gao, C. Xuan, and S.X. Tian, Nat. Chem. **8**, 258 (2016).

[18] F.H. Ómarsson, N.J. Mason, E. Krishnakumar, and O. Ingõlfsson, Angew. Chemie - Int. Ed. **53**, 12051 (2014).

[19] J.N. Bull, J.W.L. Lee, and C. Vallance, Phys. Rev. A **91**, 022704 (2015).

[20] K. Tanzer, L. Feketeová, B. Puschnigg, P. Scheier, E. Illenberger, and S. Denifl, Angew. Chemie Int. Ed. **53**, 12240 (2014).

[21] A. Amrein, R. Simpson, and P. Hackett, J. Chem. Phys. **94**, 4663 (1991).

[22] A. Amrein, R. Simpson, and P. Hackett, J. Chem. Phys. **95**, 1781 (1991).

[23] B. Baguenard, J.C. Pinaré, C. Bordas, and M. Broyer, Phys. Rev. A **63**, 023204 (2001).

[24] J.U. Andersen, E. Bonderup, and K. Hansen, J. Phys. B At., Mol. Opt. Phys. **35**, R1 (2002).

[25] W.C. Lineberger, Annu. Rev. Phys. Chem. **64**, 21 (2013).

[26] K.M. Ervin and W.C. Lineberger, in *Adv. Gas Phase Ion Chem.*, edited by N.G. Adams and L.M. Babcock (JAI Press, Greenwich, 1992), p. 121.

[27] L.-S. Wang, J. Chem. Phys. **143**, 040901 (2015).

[28] D.M. Neumark, J. Phys. Chem. A **112**, 13287 (2008).

[29] P.G. Wenthold and W.C. Lineberger, Acc. Chem. Res. **32**, 597 (1999).

[30] J.H. Hendricks, S.A. Lyapustina, H.L. de Clercq, J.T. Snodgrass, and K.H. Bowen, J. Chem. Phys. **104**, 7788 (1996).

[31] S.T. Stokes, A. Grubisic, X. Li, Y. Jae Ko, and K.H. Bowen, J. Chem. Phys. **128**, 044314 (2008).

[32] E.P. Wigner, Phys. Rev. **73**, 1002 (1948).

[33] U. Fano and D. Dill, Phys. Rev. A **6**, 185 (1972).

[34] A.T.J.B. Eppink and D.H. Parker, Rev. Sci. Instrum. **68**, 3477 (1997).

[35] D.W. Chandler and P.L. Houston, J. Chem. Phys. **87**, 1445 (1987).

[36] M.N.R. Ashfold, N.H. Nahler, A.J. Orr-Ewing, O.P.J. Vieuxmaire, R.L. Toomes, T.N. Kitsopoulos, I.A. Garcia, D.A. Chestakov, S.-M. Wu, and D.H. Parker, Phys. Chem. Chem. Phys. **8**, 26 (2006).

[37] A.J.R. Heck and D.W. Chandler, Annu. Rev. Phys. Chem. **46**, 335 (1995).

[38] I. Powis, in *Adv. Chem. Phys.*, edited by S.A. Rice (John Wiley & Sons, 2008), pp. 267–329.

[39] K.L. Reid, Annu. Rev. Phys. Chem. **54**, 397 (2003).

[40] R.N. Zare, Mol. Photochem. **4**, 1 (1972).

[41] A. Sanov, Annu. Rev. Phys. Chem. **65**, 341 (2014).

[42] D. Khuseynov, C.C. Blackstone, L.M. Culberson, and A. Sanov, J. Chem. Phys. **141**, 124312 (2014).

[43] C.M. Oana and A.I. Krylov, J. Chem. Phys. **131**, 124114 (2009).

[44] K. Regeta and M. Allan, Phys. Rev. Lett. **110**, 203201 (2013).

[45] F. Currell and J. Comer, Phys. Rev. Lett. **74**, 1319 (1995).

[46] T. Reddish, F. Currell, and J. Comer, J. Phys. E. Sci. Instrum. **36**, 203 (1988).

[47] M. Allan, in *Abstr. Pap. Am. Chem. Soc. Vol. 251* (2016).

[48] D.B. Dao and R. Mabbs, J. Chem. Phys. **141**, 154304 (2014).

[49] C.L. Adams, H. Schneider, and J.M. Weber, J. Phys. Chem. A **114**, 4017 (2010).

[50] J. Postler, V. Vizcaino, S. Denifl, F. Zappa, S. Ralser, M. Daxner, E. Illenberger, and P. Scheier, J. Phys. Chem. A **118**, 6553 (2014).

[51] A. Stolow, A.E. Bragg, and D.M. Neumark, Chem. Rev. **104**, 1719 (2004).

[52] T. Suzuki, Annu. Rev. Phys. Chem. **57**, 555 (2006).

[53] V. Blanchet, M.Z. Zgierski, T. Seideman, and A. Stolow, Nature **401**, 52 (1999).

[54] C.Z. Bisgaard, O.J. Clarkin, G. Wu, A.M.D. Lee, O. Gessner, C.C. Hayden, and A. Stolow, Science **323**, 1464 (2009).

[55] J. Lecointre, G.M. Roberts, D.A. Horke, and J.R.R. Verlet, J. Phys. Chem. A **114**, 11216 (2010).

[56] T. Suzuki, Int. Rev. Phys. Chem. **31**, 265 (2012).

[57] A.S. Chatterley, C.W. West, G.M. Roberts, V.G. Stavros, and J.R.R. Verlet, J. Phys. Chem. Lett. **5**, 843 (2014).

[58] A.S. Chatterley, C.W. West, V.G. Stavros, and J.R.R. Verlet, Chem. Sci. **5**, 3963 (2014).

[59] C.R.S. Mooney, D.A. Horke, A.S. Chatterley, A. Simperler, H.H. Fielding, and J.R.R. Verlet, Chem. Sci. **4**, 921 (2013).

[60] D.A. Horke, A.S. Chatterley, J.N. Bull, and J.R.R. Verlet, J. Phys. Chem. Lett. **6**, 189 (2015).

[61] A.S. Chatterley, D.A. Horke, and J.R.R. Verlet, Phys. Chem. Chem. Phys. **14**, 16155 (2012).

[62] D.A. Horke, A.S. Chatterley, and J.R.R. Verlet, J. Phys. Chem. Lett. **3**, 834 (2012).

[63] J.R.R. Verlet, D.A. Horke, and A.S. Chatterley, Phys. Chem. Chem. Phys. **16**, 15043 (2014).

[64] D.A. Horke, A.S. Chatterley, and J.R.R. Verlet, Phys. Rev. Lett. **108**, 083003 (2012).

[65] J. Fenn, M. Mann, C. Meng, S. Wong, and C. Whitehouse, Science **246**, 64 (1989).

[66] W.C. Wiley and I.H. McLaren, Rev. Sci. Instrum. **26**, 1150 (1955).

[67] A.B. Wolk, C.M. Leavitt, E. Garand, and M.A. Johnson, Acc. Chem. Res. **47**, 202 (2014).

[68] X.-B. Wang and L.-S. Wang, Rev. Sci. Instrum. **79**, 073108 (2008).

[69] D.A. Horke, G.M. Roberts, J. Lecointre, and J.R.R. Verlet, Rev. Sci. Instrum. **83**, 063101 (2012).

[70] G.M. Roberts, J.L. Nixon, J. Lecointre, E. Wrede, and J.R.R. Verlet, Rev. Sci. Instrum. **80**, 053104 (2009).

[71] G.A. Garcia, L. Nahon, and I. Powis, Rev. Sci. Instrum. **75**, 4989 (2004).

[72] B. Whitaker, *Imaging in Molecular Dynamics: Technology and Applications* (Cambridge University Press, 2003).

[73] H. Nohl, W. Jordan, and R.J. Youngman, Adv. Free Radic. Biol. Med. **2**, 211 (1986).

[74] E. Cadenas, Annu. Rev. Biochem. **58**, 79 (1989).

[75] J. Johnson Inbaraj, M.C. Krishna, R. Gandhidasan, and R. Murugesan, Biochim. Biophys. Acta - Gen. Subj. **1472**, 462 (1999).

[76] W. Hillier and G.T. Babcock, Plant Physiol. **125**, 33 (2001).

[77] A.H. Millar, J. Whelan, K.L. Soole, and D.A. Day, Annu. Rev. Plant Biol. **62**, 79 (2011).

[78] S. Fukuzumi, Bull. Chem. Soc. Jpn. **79**, 177 (2006).

[79] T. Nagata, Res. Chem. Intermed. **40**, 3183 (2014).

[80] G.L. Closs and J.R. Miller, Science **240**, 440 (1988).

[81] R.A. Holroyd, J. Phys. Chem. **86**, 3541 (1982).

[82] M. Allan, Chem. Phys. **81**, 235 (1983).

[83] M. Allan, Chem. Phys. **84**, 311 (1984).

[84] K. Piech, T. Bally, T. Ichino, and J. Stanton, Phys. Chem. Chem. Phys. **16**, 2011 (2014).

[85] A.A. Kunitsa and K.B. Bravaya, J. Phys. Chem. Lett. **6**, 1053 (2015).

[86] A.A. Kunitsa and K.B. Bravaya, Phys. Chem. Chem. Phys. **18**, 3454 (2016).

[87] J. Schiedt and R. Weinkauf, J. Chem. Phys. **110**, 304 (1999).

[88] P.B. Comita and J.I. Brauman, J. Am. Chem. Soc. **109**, 7591 (1987).

[89] J. Marks, P.B. Comita, and J.I. Brauman, J. Am. Chem. Soc. **107**, 3718 (1985).

[90] C.W. West, J.N. Bull, E. Antonkov, and J.R.R. Verlet, J. Phys. Chem. A **118**, 11346 (2014).

[91] Q. Fu, J. Yang, and X.-B. Wang, J. Phys. Chem. A **115**, 3201 (2011).

[92] C.D. Cooper, W.T. Naff, and R.N. Compton, J. Chem. Phys. **63**, 2752 (1975).

[93] L.G. Christophorou, J.G. Carter, and A.A. Christodoulides, Chem. Phys. Lett. **3**, 237 (1969).

[94] P.M. Collins, L.G. Christophorou, E.L. Chaney, and J.G. Carter, Chem. Phys. Lett. **4**, 646 (1970).

[95] M.H. Stockett and S.B. Nielsen, Phys. Chem. Chem. Phys. **18**, 6996 (2016).

[96] D.A. Horke, Q. Li, L. Blancafort, and J.R.R. Verlet, Nat. Chem. **5**, 711 (2013).

[97] A. Modelli and P.D. Burrow, J. Phys. Chem. **88**, 3550 (1984).

[98] K.S. Strode and E.P. Grimsrud, Chem. Phys. Lett. **229**, 551 (1994).

[99] S.A. Pshenichnyuk, N.L. Asfandiarov, V.S. Fal'ko, and V.G. Lukin, Int. J. Mass Spectrom.

227, 281 (2003).

[100] N.L. Asfandiarov, S.A. Pshenichnyuk, A.I. Fokin, and E.P. Nafikova, Chem. Phys. **298**, 263 (2004).

[101] M.O.A. El Ghazaly, A. Svendsen, H. Bluhme, S.B. Nielsen, and L.H. Andersen, Chem. Phys. Lett. **405**, 278 (2005).

[102] S. Siegert, F. Vogeler, and R. Weinkauf, Zeitschrift Für Phys. Chemie **225**, 507 (2011).

[103] Y. Honda, M. Hada, M. Ehara, and H. Nakatsuji, J. Phys. Chem. A **106**, 3838 (2002).

[104] J. Weber, K. Malsch, and G. Hohlneicher, Chem. Phys. **264**, 275 (2001).

[105] R. Pou-Amérigo, L. Serrano-Andrés, M. Merchán, E. Ortí, and N. Forsberg, J. Am. Chem. Soc. **122**, 6067 (2000).

[106] A.R. Cook, L.A. Curtiss, and J.R. Miller, J. Am. Chem. Soc. **119**, 5729 (1997).

[107] Y.-O. Kim, Y.M. Jung, S. Bin Kim, and S.-M. Park, Anal. Chem. **76**, 5236 (2004).

[108] R.L. Gordon, D.R. Sieglaff, G.H. Rutherford, and K.L. Stricklett, Int. J. Mass Spectrom. Ion Process. **164**, 177 (1997).

[109] D.A. Horke, Q. Li, L. Blancafort, and J.R.R. Verlet, Nat. Chem. **5**, 711 (2013).

[110] V.G. Stavros and J.R.R. Verlet, Annu. Rev. Phys. Chem. **67**, 9.1 (2016).

[111] A. Kammrath, G.B. Griffin, J.R.R. Verlet, R.M. Young, and D.M. Neumark, J. Chem. Phys. **126**, 244306 (2007).

[112] A.E. Bragg, Science **306**, 669 (2004).

[113] M.H. Elkins, H.L. Williams, A.T. Shreve, and D.M. Neumark, Science **342**, 1496 (2013).

[114] J.N. Bull, C.W. West, and J.R.R. Verlet, Chem. Sci. **6**, 1578 (2015).

[115] S.A. Pshenichnyuk, A.S. Vorob'ev, N.L. Asfandiarov, and A. Modelli, J. Chem. Phys. **132**, 244313 (2010).

[116] N.L. Asfandiarov, S.A. Pshenichnyuk, A.S. Vorob'ev, E.P. Nafikova, Y.N. Elkin, D.N. Pelageev, E.A. Koltsova, and A. Modelli, Rapid Commun. Mass Spectrom. **28**, 1580 (2014).

[117] J.N. Bull, C.W. West, and J.R.R. Verlet, Phys. Chem. Chem. Phys. **17**, 16125 (2015).

[118] J.N. Bull, C.W. West, and J.R.R. Verlet, Chem. Sci. DOI: 10.1039/C6SC01062H.

[119] C.W. West, J.N. Bull, A.S. Hudson, S.L. Cobb, and J.R.R. Verlet, J. Phys. Chem. B **119**, 3982 (2015).

[120] C.W. West, A.S. Hudson, S.L. Cobb, and J.R.R. Verlet, J. Chem. Phys. **139**, 071104 (2013).

[121] A.S. Chatterley, D.A. Horke, and J.R.R. Verlet, Phys. Chem. Chem. Phys. **16**, 489 (2014).

[122] J.N. Bull, C.W. West, and J.R.R. Verlet, Phys. Chem. Chem. Phys. **17**, 32464 (2015).

[123] K.D. Jordan, V.K. Voora, and J. Simons, Theor. Chem. Acc. **133**, 1445 (2014).

[124] U. V Riss and H.D. Meyer, J. Phys. B At. Mol. Opt. Phys. **26**, 4503 (1993).

[125] U. V Riss and H.-D. Meyer, J. Phys. B At. Mol. Opt. Phys. **31**, 2279 (1998).

[126] J. Muga, J. Palao, B. Navarro, and I. Egusquiza, Phys. Rep. **395**, 357 (2004).

[127] T.-C. Jagau and A.I. Krylov, J. Phys. Chem. Lett. **5**, 3078 (2014).

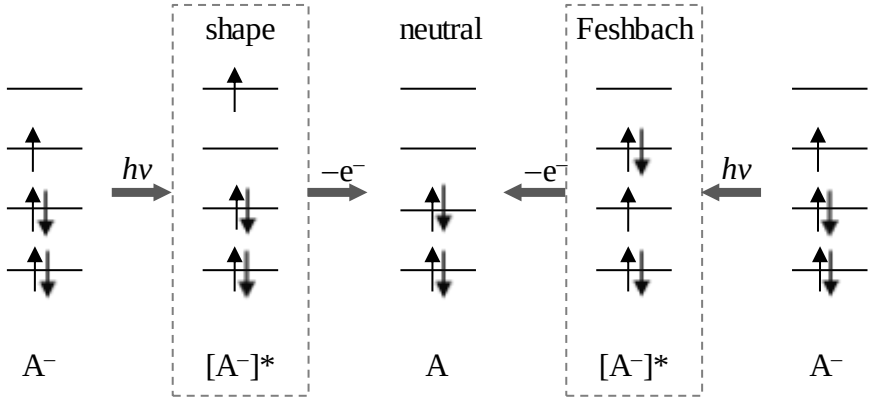

Figure 1: Electronic configurations defining shape and Feshbach resonances of a radical anion, A^-.

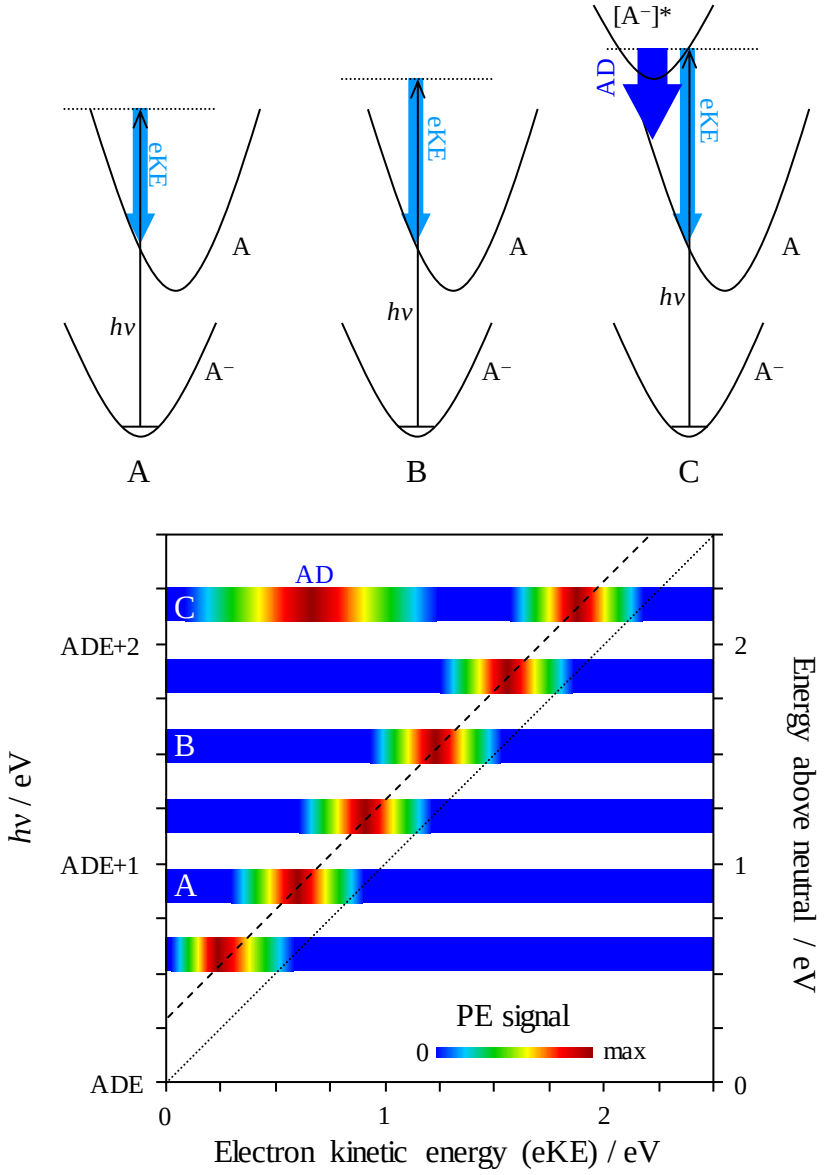

Figure 2: Pictorial representation of frequency-resolved photoelectron spectroscopy. In the top panel, the photon energy (*hν*) is increased from left to right (A to C) leading to an increase in electron kinetic energy (eKE) of the detached photoelectron. The corresponding frequency-resolved spectra are shown in the 2D graph. If *hν* is resonant with a transition that accesses a resonance of the anion, resonance autodetachment (AD) may be expected. If the lifetime of the resonance is sufficiently long, then the spectrum of the autodetachment will be at lower energy, as indicated in the 2D graph. The dashed and dotted lines with unit gradient represent the vertical and adiabatic detachment energies, respectively.

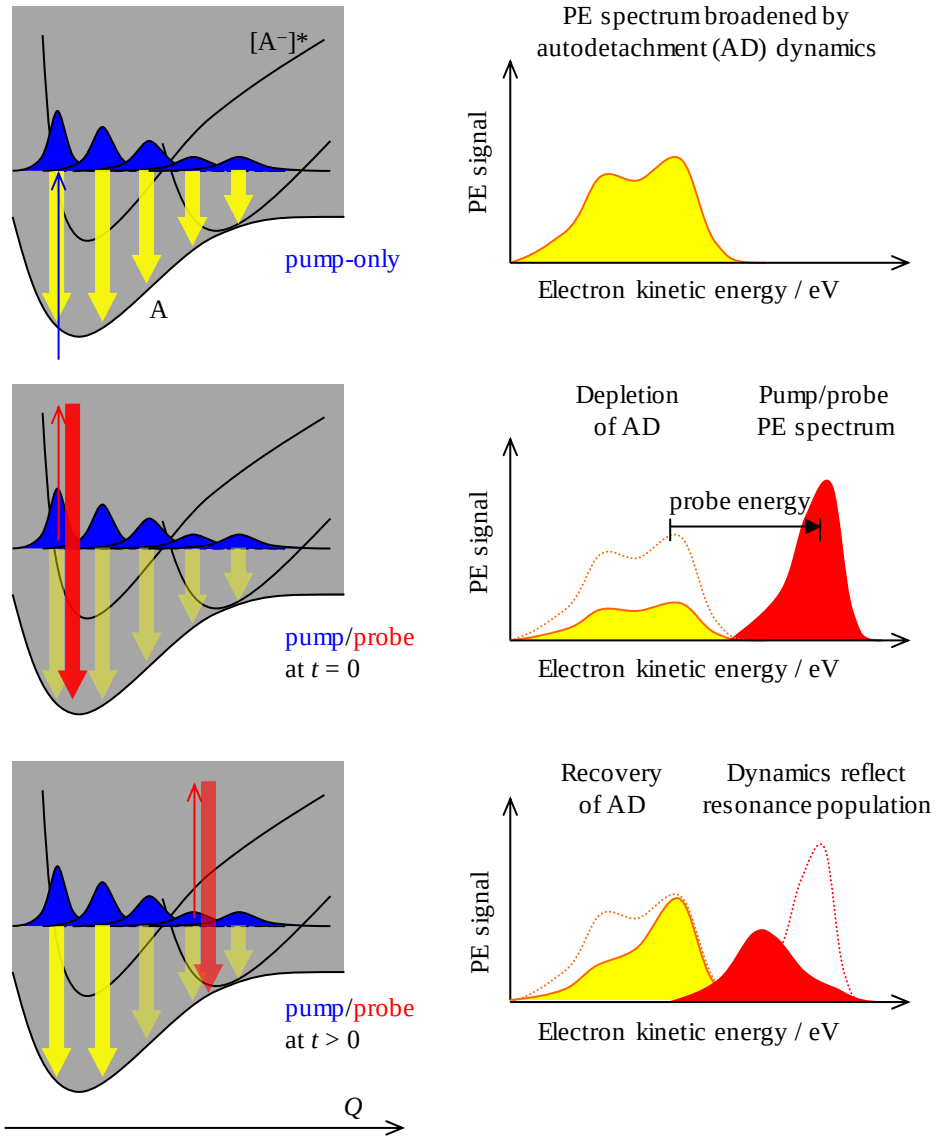

Figure 3: Pictorial representation of time-resolved photoelectron spectroscopy applied to the study of anionic resonances. In the top panel, a femtosecond pump pulse photoexcites a resonance. If the autodetachment (AD) lifetime of the resonance is long compared to the nuclear vibrations of the system, AD may occur along some intermolecular coordinate, *Q*, as indicated by the downward arrows. A delayed probe pulse can then sample population from the resonance, as shown in the middle panel, leading to the depletion in AD and the appearance electrons with higher kinetic energy. By varying the pump-probe time delay, as shown in the lower panel, the dynamics of the resonance can be probed in real-time.

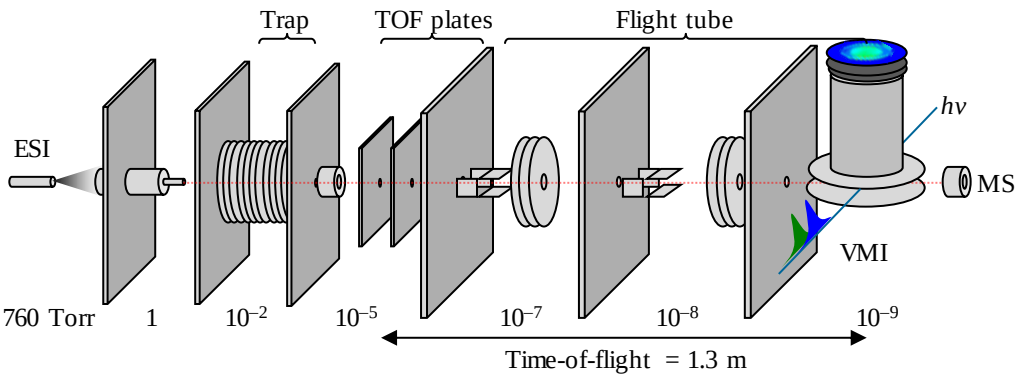

Figure 4: Schematic of the experimental arrangement to perform FAT-PI. Anions are generated by electrospray ionisation (ESI) and trapped in a ring-electrode trap. The trap is emptied into a time-of-flight (TOF) mass spectrometer (MS) and a mass-selected anion packet is intersected with light pulses (*hν*) from either a tunable nanosecond or femtosecond laser. Resulting photoelectrons are analysed using a velocity-map imaging (VMI) spectrometer. The instrument is segmented into six differentially pumped stages, achieving an ultimate pressure of 10^{-9} Torr in the detection region.

Figure 5: Structures of (a) *para*-benzoquinone (pBQ), (b) menadione (MD), and (c) coenzyme Q_0 (CQ_0).

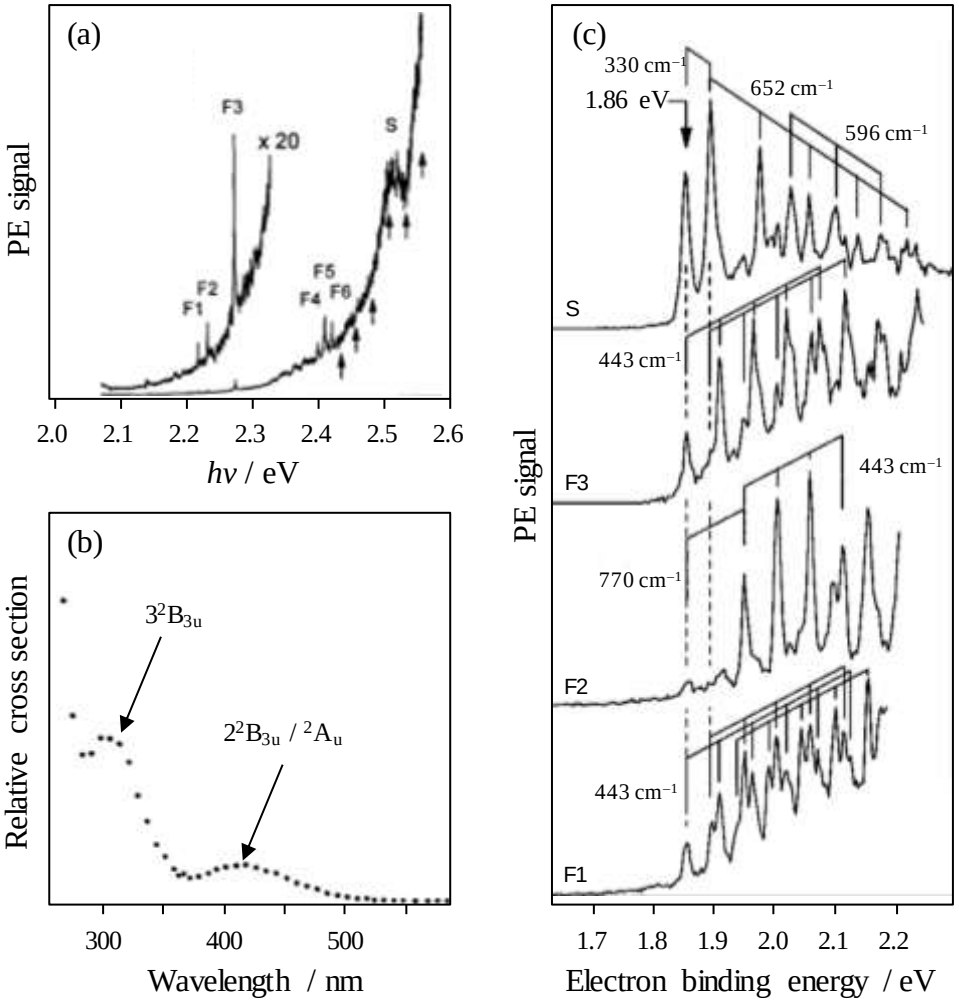

Figure 6: Photodetachment photoelectron spectra of pBQ^-. (a) and (b) show high- and low-resolution total photoelectron yield spectra. The sharp features in (a) arise from Feshbach resonances (F1 – F6) and a broad feature from the origin of the ^2A_u shape resonance (S); the low-resolution spectrum shows the relevant resonances over the first few eV of the continuum. Photoelectron spectra in (b) were taken at photon energies that are resonant with the resonances identified in (a). Panels (a) and (c) are adapted from reference 87 and (b) from reference 88.

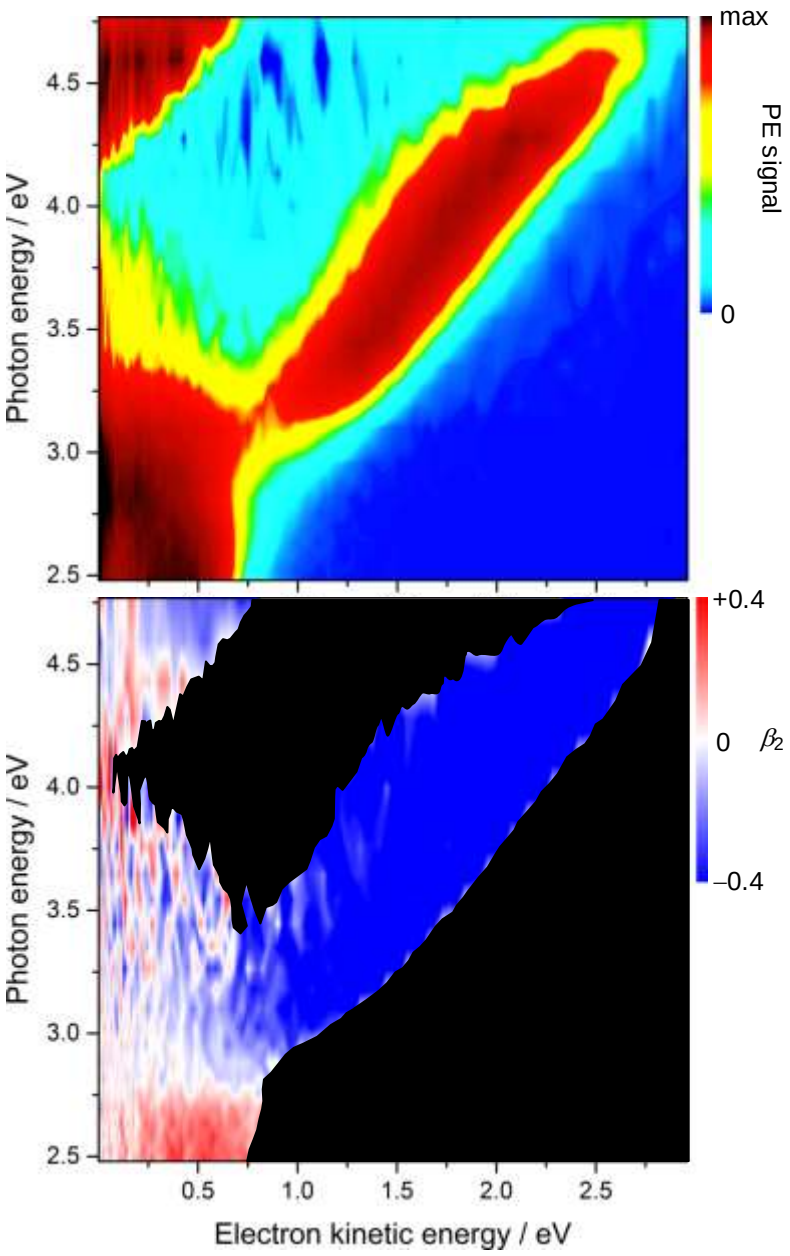

Figure 7: Frequency resolved photoelectron spectra (a) and photoelectron anisotropy parameters, β_2, (b) of pBQ^-. Adapted from reference 90.

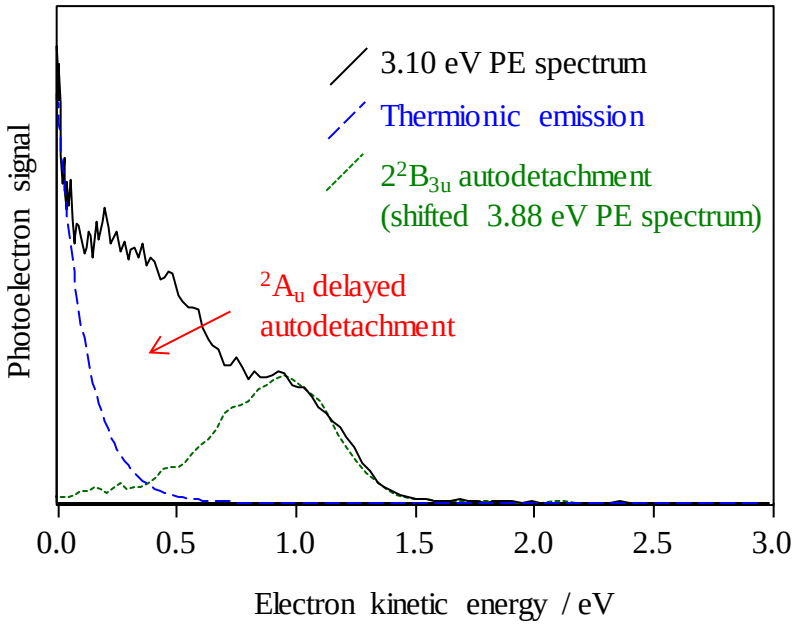

Figure 8: Photoelectron spectrum of pBQ^- recorded with *hv* = 3.10 eV (black solid line). There are three different detachment channels. Thermionic emission (blue) has the Boltzmann-like distribution centred at eKE ~ 0 eV. The photoelectron spectrum recorded with *hv* = 3.88 eV has been red-shifted by 0.78 eV, and represents the combined "direct" photodetachment and prompt autodetachment contribution from the 2^2B_{3u} resonance. The remaining signal at intermediate eKE results from autodetachment of the intermediate ^2A_u resonance following internal conversion from 2^2B_{3u}.

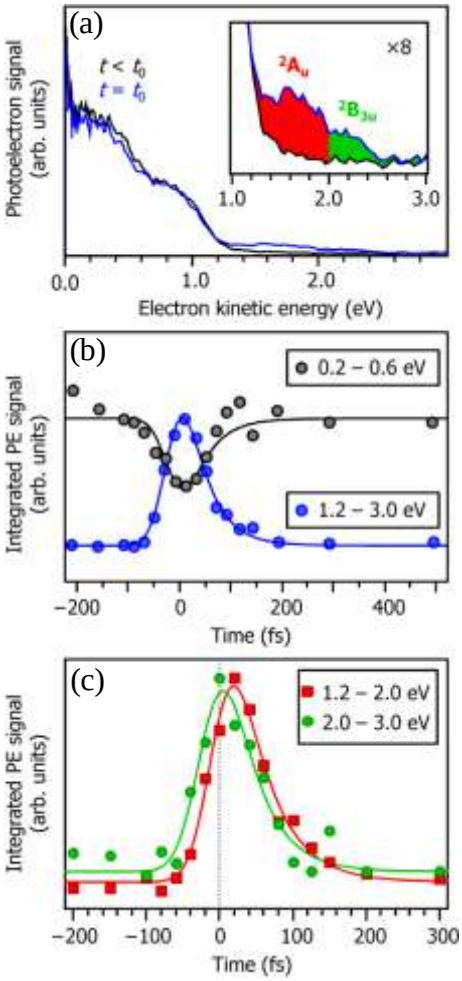

Figure 9: Time-resolved photoelectron spectroscopy of pBQ^- following excitation at *hν* = 3.10 eV (2^2B_{3u} resonance). Two representative photoelectron spectra are shown in (a) with probe arriving before the pump ($t < t_0$) and both pump and probe temporally overlapped ($t = t_0$). The inset shows an expanded view of the high-energy time-resolved feature, which can be divided into 2^2B_{3u} and ^2A_u contributions. Integral photoelectron contributions are given in (b) and (c). In (b), the two integration regions represent the pump-probe appearance signal and depletion signal. In (c), the integration regions represent the signal arising from the 2^2B_{3u} and ^2A_u resonances, as indicated in (a). Reproduced from reference 96.

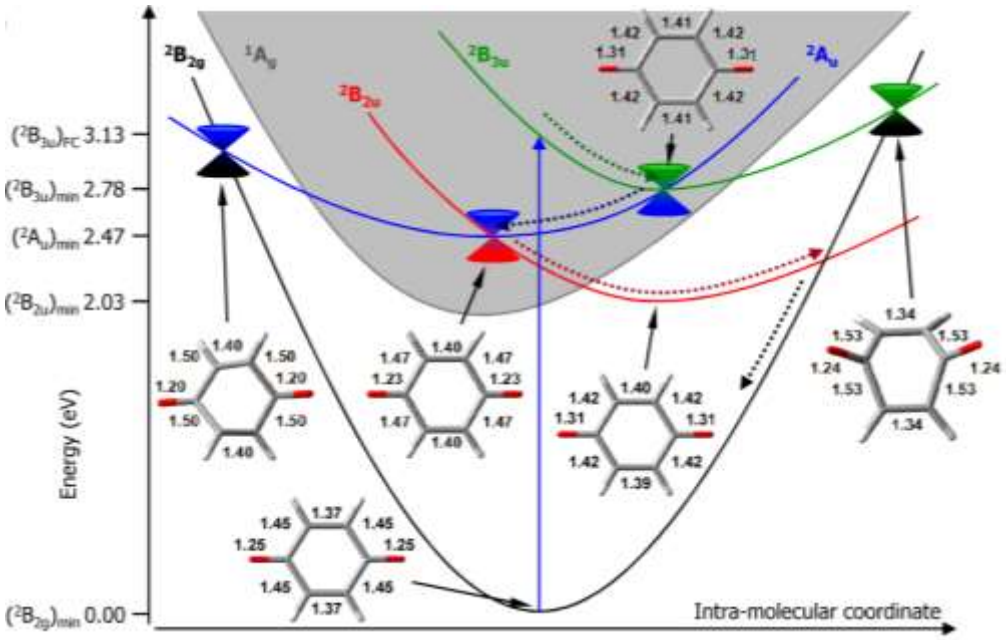

Figure 10: Calculated critical points in the pBQ^-. A conical intersection between the 2^2B_{3u} and ^2A_u resonances was located near the minimum of the 2^2B_{3u} potential energy surface, which provides an efficient pathway to internally convert to ^2A_u. Other conical intersections leading to the ground electronic state are identified. Reproduced from reference 96.

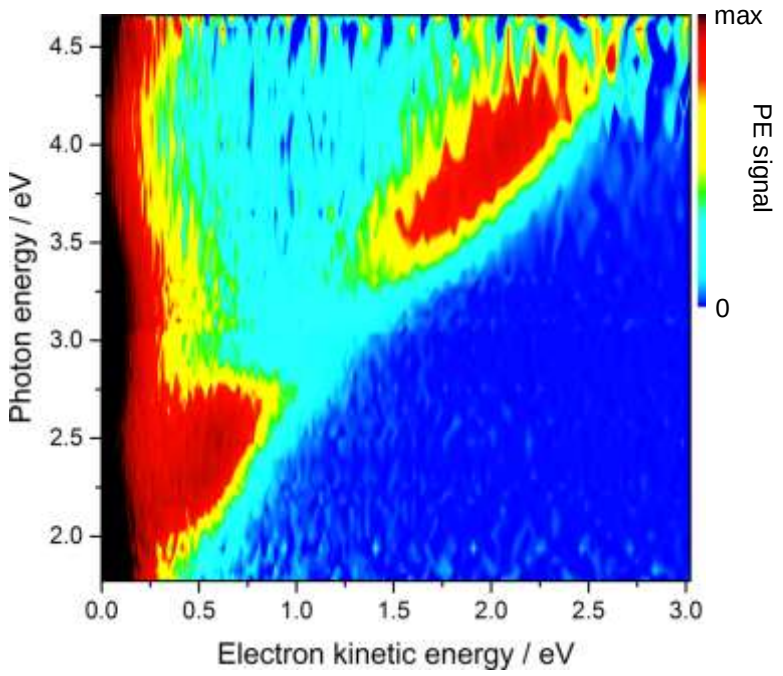

Figure 11: Frequency resolved photoelectron spectra of MD^-. Reproduced from reference 114.

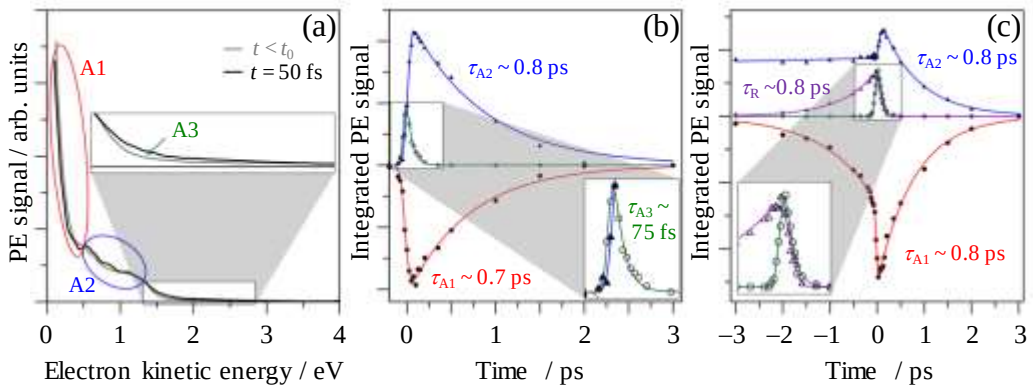

Figure 12: Time-resolved photoelectron spectroscopy of MD^- following excitation at *hv* = 3.10 eV ($3^2A''$ resonance). Representative time-resolved photoelectron spectra are shown in (a) with a 0.95 eV probe and convey the spectral changes associated with the dynamics. The time-evolution of spectral components from (a) is shown in (b) and indicates a fast decay associated with feature (A3), which leads to an intermediate feature (A2) that decays with an ~800 fs lifetime. The ground state depletion (A1) recovers with approximately the same lifetime. Panel (c) shows the results from a similar analysis as in (b) but using a 1.55 eV probe. This pump-probe scheme reveals identical dynamics in the positive time delay direction (3.10 eV pump, 1.55 eV probe), but allows the intermediate (A2) to be directly characterised in the negative time delay direction (1.55 eV pump, 3.10 eV probe). Adapted from reference 114.

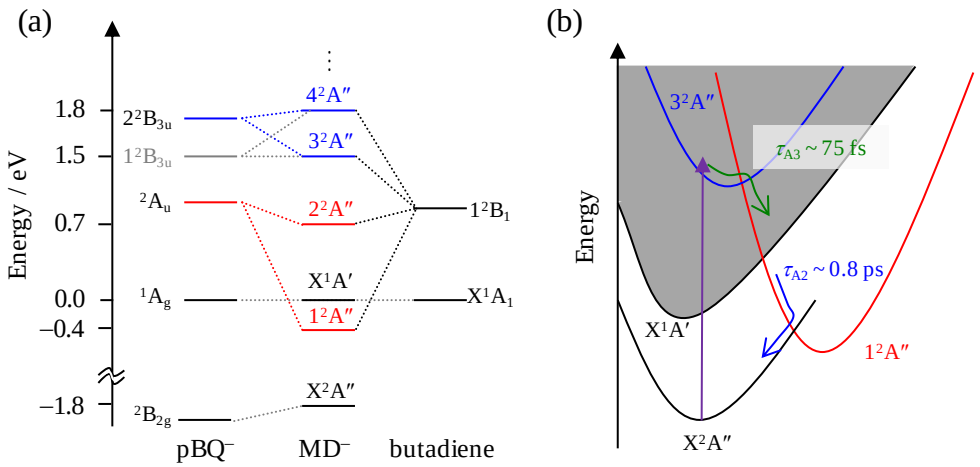

Figure 13: (a) Correlation diagram of ground and excited electronic state energetics of MD^-, pBQ^-, and *cis*-butadiene. A schematic summary of the excited state dynamics of MD^- is given in (b), showing the initially excited $3^2A''$ resonance internally converts to the bound electronic $1^2A''$ state in ~75 fs., which then internally converts to the ground electronic state on a slower ~800 fs timescale. The ground electronic state detaches the electrons as thermionic emission.

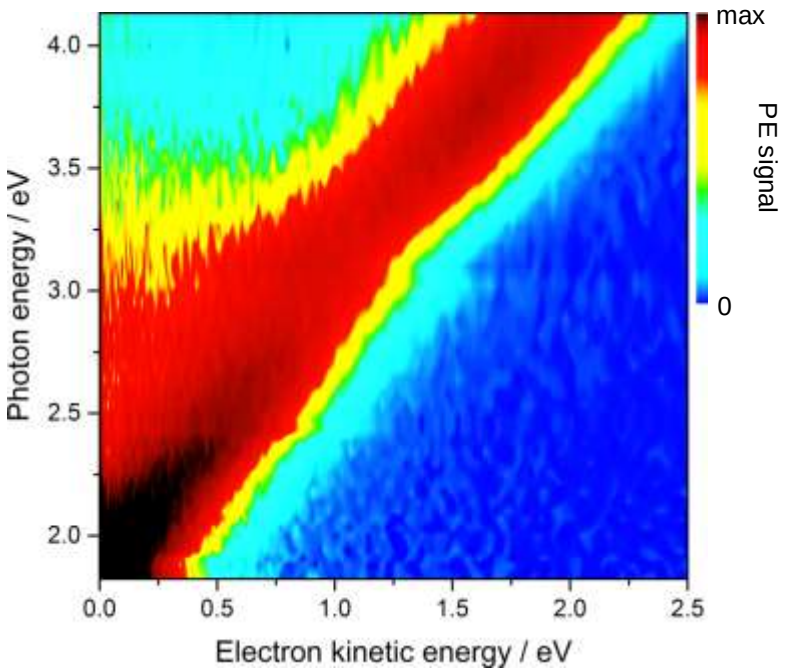

Figure 14: Frequency resolved photoelectron spectra of CQ_0^-. Adapted from reference 117.

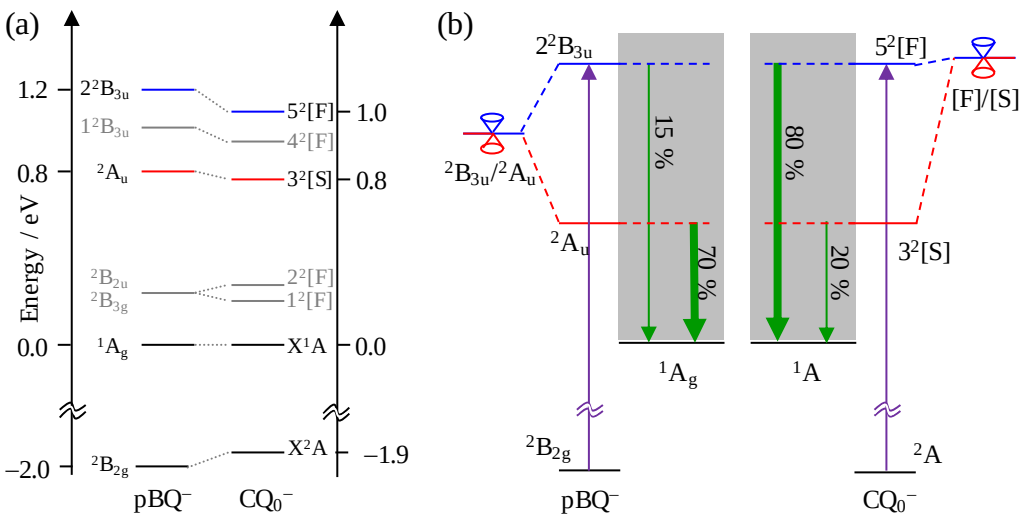

Figure 15: (a) Correlation diagram of ground and excited electronic state energetics of pBQ^- and CQ_0^-. Electron detachment and internal conversion pathways and branching ratios are summarised in (b). For pBQ^-, the majority of population decays to the lower-lying resonance mediated by a conical intersection that is accessible along the Franck-Condon active modes. In contrast, the conical intersection in CQ_0^- is not as readily accessed and most 5^2[F] population autodetaches. Adapted from reference 117.